P Wave Azimuthal Anisotropic Tomography in Northern Chile: Insight Into Deformation in the Subduction Zone

Zhouchuan Huang[1,2] , **Frederik Tilmann**[2,3] , **Diana Comte**[4,5], and **Dapeng Zhao**[6]

[1]School of Earth Sciences and Engineering, Nanjing University, Nanjing, China, [2]GeoForschungsZentrum Potsdam, Potsdam, Germany, [3]Seismology, Freie Universität Berlin, Berlin, Germany, [4]Departamento de Geofisica, Facultad de Ciencias Fisicas y Matematicas, Universidad de Chile, Santiago, Chile, [5]Advanced Mining Technology Center, Facultad de Ciencias Fisicas y Matematicas, Universidad de Chile, Santiago, Chile, [6]Department of Geophysics, Tohoku University, Sendai, Japan

Abstract Based on a large data set of local body wave travel times, we determined the first 3-D model of azimuthal *P* wave anisotropic tomography of northern Chile in order to study the deformation in the subduction zone. Our results indicate different deformation patterns in the overriding lithosphere, mantle wedge, and the subducting Nazca slab as well as significant along-arc variations. Radiating fast velocity directions (FVDs) around the rupture zone of the 2014 Iquique earthquake (Mw 8.2) are notable in the crust, which may reflect the specific crustal extension induced by a point-like stress source in the form of a fully locked asperity at the plate interface. In most of the study region, FVDs in the mantle wedge are trench normal, which we interpret to have resulted from mantle wedge flow driven by the oceanic plate subduction. However, trench-parallel FVDs are found beneath the northern segment, which may imply the occurrence of B-type olivine fabrics in the cold forearc mantle. Strong along-arc variations are also observed in the subducting slab, which may reflect intraslab heterogeneity and change in the slab geometry. In the northern segment, slab bending induces generally trench-normal extension and leads to trench-normal FVDs in the upper part of the slab. In contrast, in the southern segment, flat slab subduction and thus slab unbending dominate, producing trench-normal compression and trench-parallel FVDs instead. Along the subducting slab interface, FVDs change from trench-parallel to trench-normal in the downdip direction, which may indicate the first-order transition from compression in the locking area to dominant shear in the decoupling area along the slab interface.

1. Introduction

Northern Chile has been experiencing subduction of the Nazca plate since Jurassic times (Figure 1a; Allmendinger & González, 2010). The forearc region is composed of a series of N-S magmatic arcs, which migrated eastward, that is, from the oldest Jurassic arc in the Coastal Cordillera to the current volcanic arc in the Western Cordillera (Figure 1c). At present the Nazca plate is subducting beneath the South American plate at a rate of ~7 cm/year (Angermann et al., 1999). The plate convergence has induced significant contraction in the overriding plate (Kendrick et al., 2001; Métois et al., 2016). However, many anomalous EW striking reverse faults and NS striking normal faults developed in the Coastal Cordillera have attracted special attention and indicate that the stress field cannot be simply described by E-W compression (Allmendinger et al., 2005; Cortés-Aranda et al., 2015). The development of these faults may be closely related to the curvature of the continental margin and the interplate locking at the plate interface (Allmendinger et al., 2005; Allmendinger & González, 2010; Bevis et al., 2001; Cortés-Aranda et al., 2015; Gephart, 1994).

The rapid convergence near this plate boundary has produced many large earthquakes in the past decades. A relatively recent rupture is the Iquique earthquake (Mw 8.2), which occurred on 1 April 2014 (Figure 1a). However, a larger event is still expected since northern Chile and southern Peru have experienced an Mw 8.7 earthquake in 1868 and an Mw 8.9 earthquake in 1877 (Comte & Pardo, 1991). Modeling of GPS (Global Positioning System) and InSAR (Interferometric Synthetic Aperture Radar) data suggests that during the interseismic, cycle the plate interface in northern Chile is generally locked to 35-km depth with a transition zone between 35- and 55-km depth (Figure 1b; Li et al., 2015; Métois et al., 2016). The along-arc variations are significant, though. The plate interface is highly locked beneath the Tocopilla segment, while it is less coupled beneath the Iquique segment (Figure 1b; Ortega-Culaciati et al., 2015). A deeper isolated, highly locked
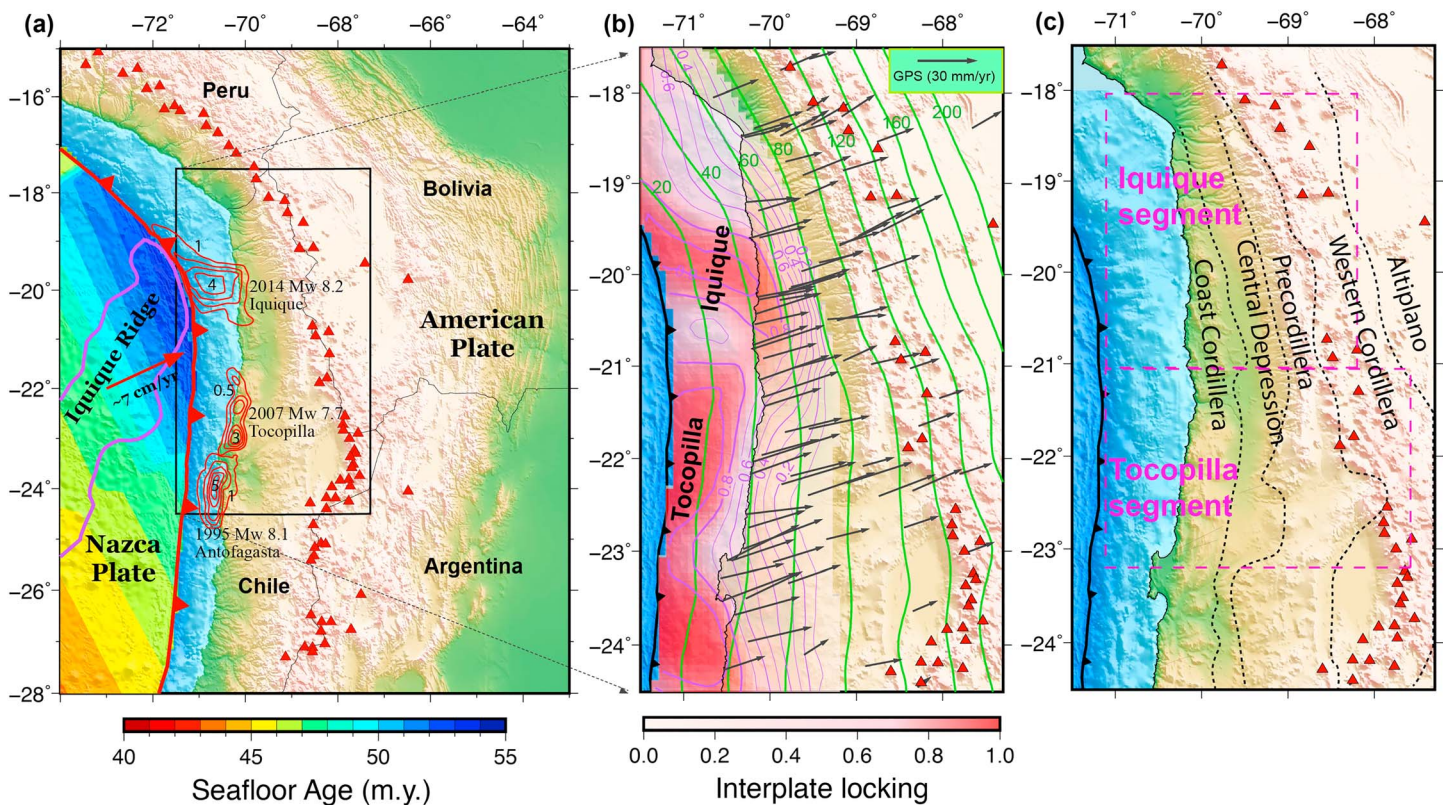
Figure 1. (a) Tectonics of northern Chile. The bold red line denotes the trench; the red arrow shows the subduction direction (Angermann et al., 1999). Yellow to blue colors denote the age of the lithosphere (Mueller et al., 2008). The purple line outlines the Iquique Ridge. The red contour lines show the rupture areas of the 2014 Iquique (Mw 8.2), 2007 Tocopilla (Mw 7.7), and the 1995 Antofagasta (Mw 8.1) earthquakes (Chlieh et al., 2004; Li et al., 2015; Schurr et al., 2012). The red triangles denote active volcanoes. (b) Pink and red colors with purple contour lines show the interplate-locking degrees along the plate interface (Li et al., 2015). The black arrows show GPS velocities in northern Chile (Kreemer et al., 2014; Métois et al., 2016) with a scale shown in the top right inset. The green contour lines show the depths of the subducting plate interface (or the upper boundary of the subducting slab; Tassara & Echaurren, 2012). (c) The dashed gray lines are boundaries between the tectonic units in northern Chile (Mpodozis et al., 2005). Magenta dashed rectangles define the two segments referred to in the text.

asperity surrounded by creeping areas has been identified offshore near Iquique (Figure 1b; Li et al., 2015). The interplate locking, which extends beneath the Coastal Cordillera, also with notable along-arc variations, may induce significant deformation near the plate boundary, especially in the overriding South American plate (Saillard et al., 2017).

There have been several studies on the three-dimensional (3-D) velocity structure of the northern Chile subduction zone (e.g., Comte et al., 2016, Graeber & Asch, 1999, Husen et al., 2000, Masson & Delouis, 1997, Schurr et al., 2006). A high-velocity slab is clearly revealed by all these studies (e.g., Comte et al., 2016, Masson & Delouis, 1997). A thin layer of low velocity and high Vp/Vs ratio is visible atop the subducting slab in some of the previous results, which may represent the subducted oceanic crust (e.g., Comte et al., 2016, Husen et al., 2000). The supraslab mantle (or mantle wedge) beneath the forearc region is also characterized by low velocities and high Vp/Vs ratios, probably indicating increased water content released from the subducting slab (e.g., Comte et al., 2016, Graeber & Asch, 1999). Attenuation tomography provides additional information on the structures beneath northern Chile (e.g., Haberland & Rietbrock, 2001, Schurr et al., 2003). The crust and upper mantle beneath the forearc as well as the subducting slab are generally characterized by low attenuation (high Qp), being consistent with a low temperature there (Haberland & Rietbrock, 2001; Schurr et al., 2003). In contrast, high attenuation (low Qp) anomalies exist in the mantle wedge beneath the active volcanoes, which reflects high-temperature, more water, and probably partial melting under the magmatic arc (e.g., Schurr et al., 2003).

Seismic anisotropy can be used to constrain the deformation patterns in the Earth's crust and upper mantle (Savage, 1999; Mainprice, 2007; Plomerová & Babuška, 2010; Sun et al., 2012; Huang, Gung, et al., 2015).

It describes a phenomenon that seismic velocities are different for different propagation directions (for P and S waves) or polarization directions (for S wave). There are two main mechanisms causing seismic anisotropy. Brittle deformation in the shallow crust can result in preferential orientation of cracks, which induces detectable anisotropy, so-called shaped preferred orientation (SPO; Crampin & Peacock, 2005). Dislocation creep aligns the constituent minerals such as amphibole and mica in the lower crust and olivine in the upper mantle, causing crystallographic preferred orientation (CPO; Ji et al., 2015; Karato et al., 2008). The fast velocity direction (FVD for P wave) or fast polarization direction (FPD for S wave) can thus be used to study the preferred orientations of structures or minerals. In general, the SPO from cracks would result in FVDs and FPDs paralleling to the cracks (i.e., perpendicular to the direction of maximum extension), while the CPO would produce FVDs and FPDs parallel to the direction of maximum extension for most crustal and mantle lithologies. However, different types of olivine fabrics develop in the mantle depending on pressure, temperature, and water content (see Karato et al., 2008, for a review). For most types of fabrics (e.g., A, C, D, and E), the fast orientation is parallel to the maximum extension, which is aligned with the maximum-shear direction for large shear strains (Karato et al., 2008). For olivine under narrow conditions of high differential stress and water content, it is also possible for the slow axis to align with the shearing direction, which is called B-type anisotropy (e.g., Jung & Karato, 2001), but its relevance to the interpretation of anisotropy in subduction zone settings is still controversial.

P wave anisotropic tomography is an effective method to reveal high-resolution 3-D velocity and anisotropic structures (see a recent review by Zhao et al., 2016). It has been applied to many collision and subduction zones (e.g., Eberhart-Phillips & Henderson, 2004; Eberhart-Phillips & Reyners, 2009; Huang et al., 2011; Huang, Zhao, et al., 2015; Ishise & Oda, 2005; Koulakov et al., 2015; Liu & Zhao, 2017; Wang & Zhao, 2008; Wei et al., 2015; Wei et al., 2016). In northeastern Japan, abundant high-quality data recorded by a dense seismic network allowed this method to resolve trench-normal anisotropy in the mantle wedge and trench-parallel anisotropy in the subducting slab, which could arise from the mantle wedge corner flow and slab bending and unbending, respectively (Huang, Zhao, et al., 2015; Liu & Zhao, 2016; Wang & Zhao, 2008). This method is also applied to reveal anisotropy along the upper boundary of the slab (Huang et al., 2011; Liu & Zhao, 2017), which provides important information on the deformation in the subduction megathrust zone.

In this study, we determine the first model of P wave azimuthal anisotropic tomography of the northern Chile subduction zone based on arrival time data of local earthquakes. Our high-resolution 3-D anisotropic model is used to analyze the deformation within the different structural elements of the subduction zone, that is, continental lithosphere, mantle wedge, and the subducting slab. Our results also provide new constraints on the deformation pattern of the megathrust zone along the slab interface.

2. Data and Method

We used P and S wave arrival times from 14,695 local earthquakes recorded at 360 stations (Figure 2); the same data set (in addition to ambient noise observations) has been used by Comte et al. (2016) for isotropic travel time tomography. The stations belong to different networks deployed over a period of 25 years (see Comte et al., 2016 and Table S1 in the supporting information for details). All earthquakes used in the inversion have at least 15 P and S arrival times, which were all picked manually. Uncertainties of the P wave arrival times are estimated to be 0.1–0.5 s, while those of S wave data are about twice as large (Comte et al., 2016). Due to the limited distribution of seismic stations and earthquakes, we can only resolve P wave velocity heterogeneities and anisotropy in the forearc region. We do not invert for the S wave velocities, but the S wave data are used for the earthquake relocation during the inversion.

Traveltime seismic tomography for 3-D isotropic velocities relates the observed traveltime residuals (r) to perturbations of hypocentral parameters (i.e., hypocenter $\Delta\varphi_e$, $\Delta\lambda_e$, Δh_e, and origin time ΔT_e) and 3-D velocity perturbations (ΔV) relative to a 1-D reference velocity model. The P wave is assumed to travel with the same velocity (V_P) in all directions (the corresponding slowness is defined as $S_0 = 1/V_P$). For weak azimuthal anisotropy with hexagonal symmetry, the variation of V_P with the azimuth of wave propagation (ϕ) can be written as a linear combination of terms proportional to $\sin2\phi$ and $\cos2\phi$ (Backus, 1965; Raitt et al., 1969). A simple expression for Pn wave slowness is (Hearn, 1996):
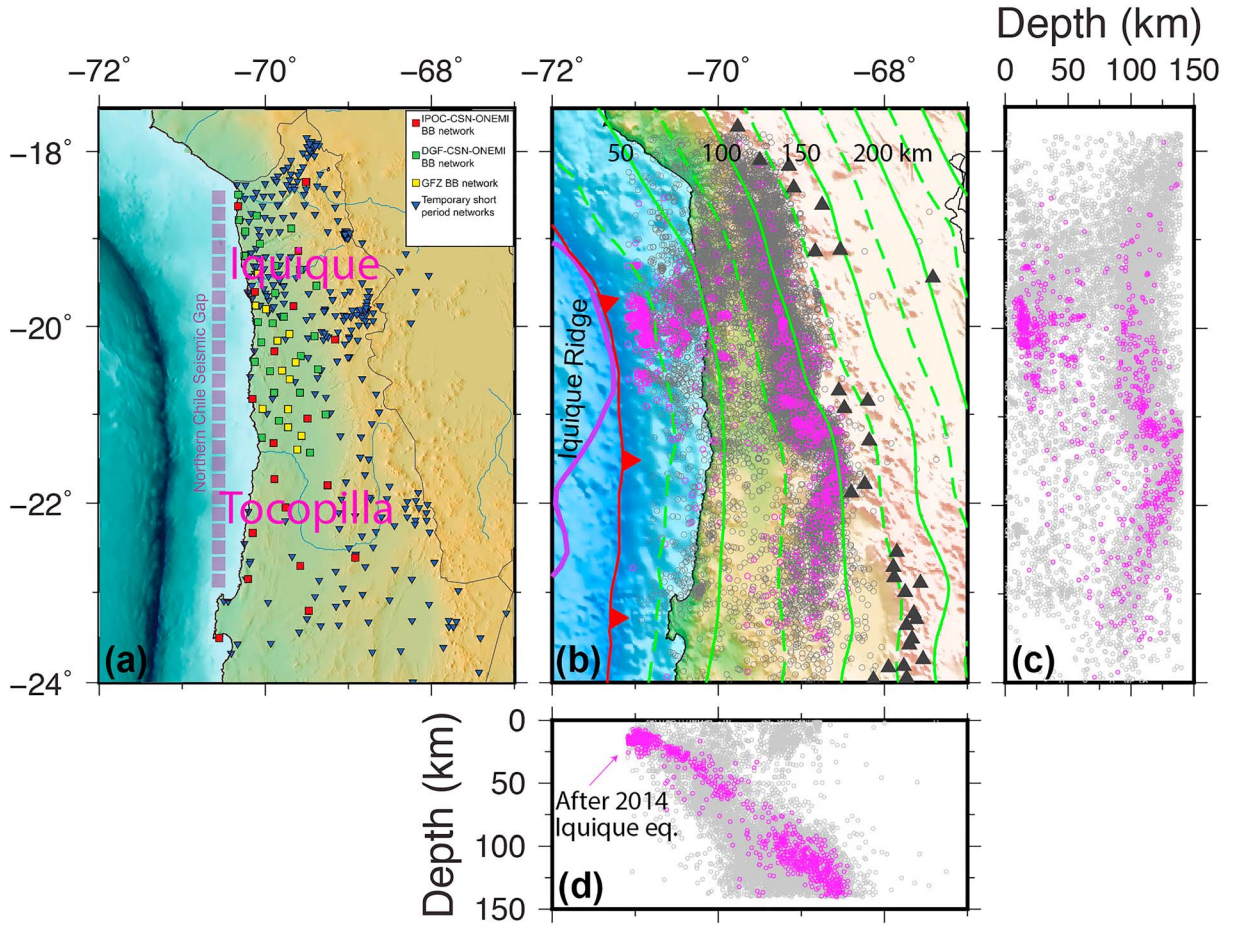
Figure 2. (a) Seismic stations and (b) events used in this study. The gray and magenta circles show the events which occurred before and after the 2014 Iquique earthquake, respectively. For the other labeling see Figure 1. (c) N-S and (d) E-W vertical cross sections showing the hypocentral distributions.

$$S(\phi) = S_0 + M\cos2(\psi-\phi) = S_0 + A\cos2\phi + B\sin2\phi \tag{1}$$

Here $M = \sqrt{A^2 + B^2}$ is related to the strength of anisotropy, and ψ is the FVD. The parameters A and B describe the azimuthal anisotropy (see Wang & Zhao, 2008, for details); specifically, the anisotropic amplitude (α, i.e., the strength of anisotropy) is given by

$$\alpha = \frac{V_f - V_s}{2V_0} = \frac{M}{S_0 - M^2/S_0} \tag{2}$$

and FVD (ψ)

$$\psi(A,B) = \begin{cases} \dfrac{1}{2}\tan^{-1}\left(\dfrac{B}{A}\right) + \begin{cases} \dfrac{\pi}{2}, A>0 \\[2mm] 0, A<0 \end{cases} \\[6mm] \left.\begin{array}{l} -\dfrac{\pi}{4}, B>0 \\[2mm] \dfrac{\pi}{4}, B<0 \end{array}\right\}, A=0 \end{cases} \tag{3}$$

where V_f and V_s denote P wave velocities in the fast and slow velocity directions, respectively, and V_0 is the average velocity.

More generally, for a P wave ray with incidence angle i, equation (1) was further extended to (e.g., Eberhart-Phillips & Henderson, 2004)

$$S(\phi) = S_0 - \cos^2 i \sqrt{A^2 + B^2} + \sin^2 i (A\cos2\phi + B\sin2\phi) \tag{4}$$

for media with a hexagonal symmetry and a horizontally oriented, slow symmetry axis.

Thus, the equations for travel time residuals for weak P wave azimuthal anisotropy are

$$r = \frac{\partial T}{\partial\varphi_e}\cdot\Delta\varphi_e + \frac{\partial T}{\partial\lambda_e}\cdot\Delta\lambda_e + \frac{\partial T}{\partial h_e}\cdot\Delta h_e + \Delta T_e + \sum_{n=1}^{N}\left(\frac{\partial T}{\partial S_n}\cdot\Delta S_n\right) + \sum_{m=1}^{M}\left(\frac{\partial T}{\partial A_m}\cdot\Delta A_m + \frac{\partial T}{\partial B_m}\cdot\Delta B_m\right) \tag{5}$$

where $\partial T/\partial\varphi_e$, $\partial T/\partial\lambda_e$, and $\partial T/\partial h_e$ are partial derivatives of travel time with respect to the hypocentral parameters (Engdahl & Lee, 1976), and $\partial T/\partial S_n$ is the partial derivative of travel time with respect to the velocity at each grid node ($n = 1, 2, ..., N$) for the isotropic Vp structure (Thurber, 1983), and $\partial T/\partial A_m$ and $\partial T/\partial B_m$ are partial derivatives of travel time with respect to the anisotropic parameters (A and B) at each grid node ($m = 1, 2, ..., M$) for Vp anisotropy (Eberhart-Phillips & Henderson, 2004; Eberhart-Phillips & Reyners, 2009; Wang & Zhao, 2008). Note that the number of grid nodes for the isotropic and anisotropic Vp structures may be chosen differently, because the anisotropic term is usually resolved with a lower resolution.

The assumption of hexagonal anisotropy with a horizontal symmetry axis is a computational necessity, as the resolution power of the data is unable to constrain more complicated anisotropy. However, at least the assumption of hexagonal symmetry is a justified simplification. The dominant minerals in the upper mantle, olivine, and enstatite show visible seismic anisotropy. Browaeys and Chevrot (2004) decomposed the elastic tensor into a sum of orthogonal tensors that belong to different symmetry classes and found that hexagonal symmetry accounts for ~75% and >50% of the total anisotropy for olivine and enstatite, respectively. Furthermore, the alignment of olivine in the mantle is not perfect along all three axes, and the inherent anisotropy of several minerals combines in such a way as to make the typical mantle and crustal petrofabric even closer to hexagonal. For example, Becker et al. (2006) confirmed that the hexagonal approximation for seismic anisotropy may capture ~80% of the total anisotropy in the upper mantle. Therefore, the assumption of hexagonal symmetry is suitable. However, inclined hexagonal symmetry is not unusual, particularly beneath continents (due to fossil anisotropy in complex folds; e.g., Babuška et al., 1993; Plomerová & Babuška, 2010) and subduction zones (due to 3-D mantle flow; e.g., Huang, Zhao, et al., 2015; Wang & Zhao, 2013). Therefore, in this study, in order to reduce the influence of inclined symmetry, we only used subhorizontal ray segments ($60° < i < 120°$, i.e., within 30° angle from horizontal) to constrain the P wave azimuthal anisotropy. A certain biasing effect due to nonhorizontal alignment of the symmetry axis cannot be excluded completely, of course, but the overall spatial organization of the strikes of possibly tilted symmetry axes is still expected to be recovered.

We applied the method of Zhao et al. (1992) and Wang and Zhao (2008) to invert the arrival-time data for 3-D isotropic Vp structure and P wave azimuthal anisotropy simultaneously. The starting isotropic velocity models are deduced from the 1-D average of the previous body wave tomography (Figure 3a; Comte et al., 2016); anisotropy is not considered at this stage. Seismic velocity discontinuities, that is, an intracrustal discontinuity, the continental Moho, and the upper boundary of the subducting slab (or the plate interface), are included in the starting model (Figures 3b–3g) according to the model of Tassara and Echaurren (2012). We also added initial velocity anomalies in the 1-D starting model to represent the subducting slab (Figures 3b–3d), that is, 4% for P wave and 6% for S wave. This prior information allows us to trace more accurately waves refracted beneath the Moho and through the subducting slab (Figure 3c). We set up two grids to express the structures in the modeling space, one for the 3-D isotropic V_P structure and the other for its azimuthal anisotropy. The lateral grid intervals are ~25 and ~33 km for isotropic and anisotropic grids, respectively. The grid meshes are set at depths of 10, 25, 40, 60, 80, 100, 120, 140, and 160 km. The perturbations of isotropic Vp and anisotropy parameters (A, B) at any point in the model are calculated by linear interpolation of their perturbations at the eight grid nodes surrounding that point. We used the 3-D ray tracing technique of Zhao et al. (1992) in isotropic media, which combines the pseudo-bending algorithm (Um & Thurber, 1987) and Snell's law to compute theoretical travel times and ray paths, and thus derive the partial derivatives of travel time with respect to hypocentral parameters, isotropic Vp perturbations, and anisotropy parameters. The LSQR algorithm (Paige & Saunders, 1982) with the parameter-separation scheme (Pavlis & Booker, 1980) is applied to solve the resulting kernel equations. Smoothing and damping regularizations are adopted to suppress dramatic short-scale variations of the unknown parameters (Lees &
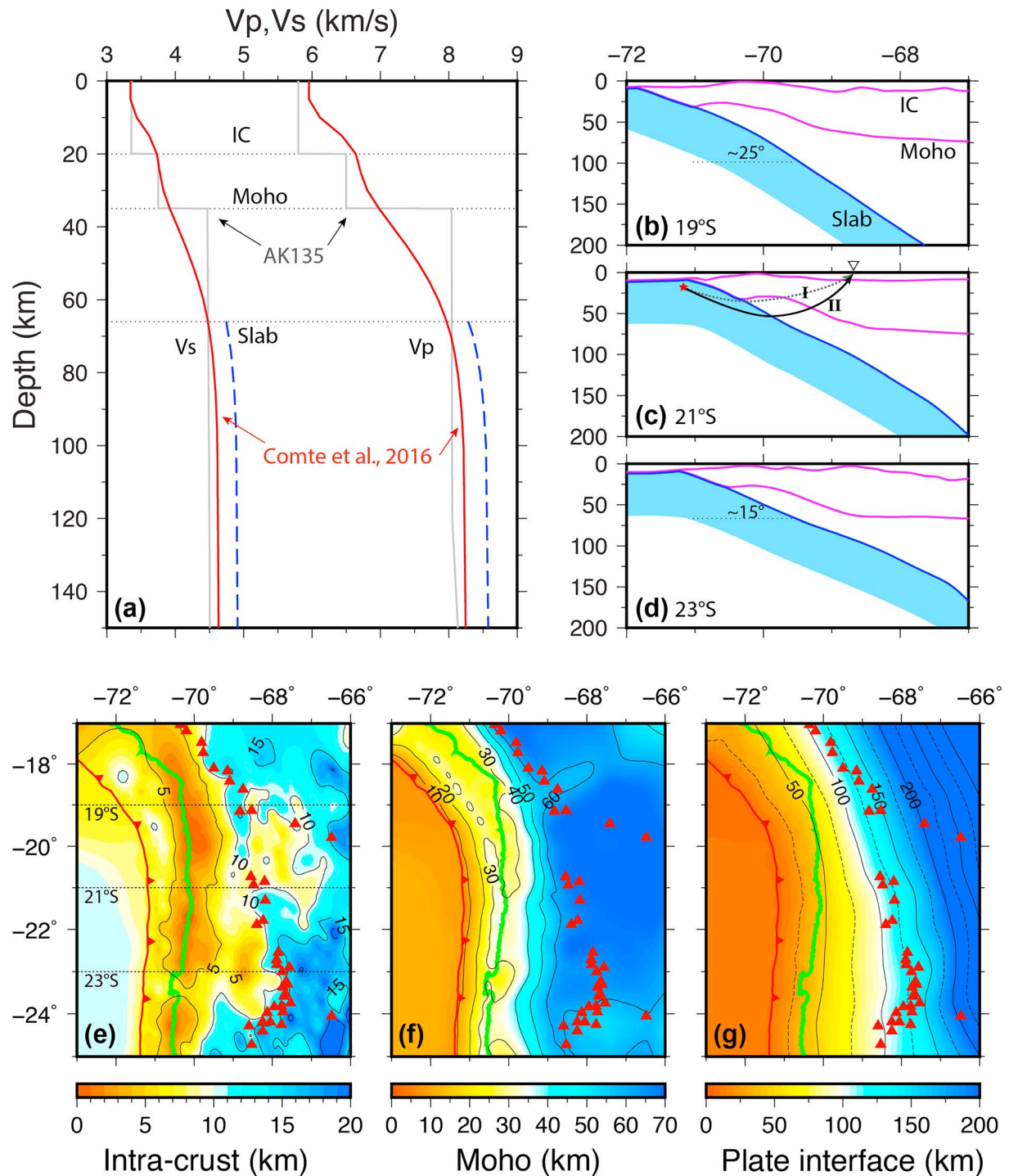
Figure 3. (a) The starting velocity model (red lines) used in this study, which is derived from the lateral average of a previous seismic tomography model (Comte et al., 2016). The gray lines show the global AK135 1-D velocity model (Kennett et al., 1995) for reference. The horizontal dashed lines show the reference depths of the intracrustal discontinuity (IC), Moho, and the upper boundary of the subducting Nazca slab as shown in (b–g). The dashed blue lines (a) indicate the initial velocities in the subducting slab (b-d), which has 4% higher Vp and 6% higher versus (b–d) three E-W vertical cross sections showing the depths of the major discontinuities beneath northern Chile (i.e., IC, Moho, and slab surface). Symbols I and II show the conceptual ray paths without and with the initial high-velocity slab. (e–g) Depth distributions of the intracrustal discontinuity, the Moho, and the upper boundary of the subducting Nazca slab in northern Chile (Tassara & Echaurren, 2012). The red and green lines denote the northern Chile trench and coast, respectively. The red triangles denote the active volcanoes.

Crosson, 1989). We used a uniform damping parameter but different smoothing parameters for the isotropic and anisotropic structures because they are expressed by different sets of grid nodes. We carried out five iterations during the inversion, and the ray paths are updated in each iteration. In addition, all the earthquakes are relocated with the newly determined 3-D Vp model after each iteration; S wave velocities are not changed in the inversion.

3. Results

3.1. Checkerboard Resolution Test

Figure 4 shows the distribution of ray paths between the stations and events used in the study. In most regions between the coast and volcanoes, the accumulated partial derivatives (of traveltime with respect to isotropic slowness perturbations) at the grid nodes are larger than 100 km, suggesting good ray coverage. The ray paths also cover the oceanic region between the trench to the coast in the Iquique segment (i.e., 18°S–21°S), thanks to the use of many aftershocks of the 2014 Iquique earthquake (Mw 8.2). In the crust, the ray coverage is poor in the southeastern part of the study area due to the small number of stations and shallow events there. In Figure 4, we also show ray ellipses, which reflect the (ray) azimuthal coverage, with large aspect ratios indicating poor azimuthal coverage and vice versa (see Huang, Zhao, et al., 2015, for more details). Azimuthal anisotropy can only be resolved where the azimuthal coverage is good, because strong trade-off between isotropic velocity and anisotropy otherwise creates artifacts in both isotropic and anisotropic models (Huang, Zhao, et al., 2015). In the shallow parts of the model (i.e., 10- to 40-km depths) the azimuthal coverage is good. However, in deeper layers (i.e., 60- to 100-km depths) between 18°S and 21°S, the dominant ray azimuths are nearly N-S, generally following the strike of the coastline, which could induce significant artifacts. In this case, comprehensive synthetic tests are necessary to estimate the robustness of even major features.

We conducted checkerboard resolution tests (CRT) to evaluate the resolution power of our data set. First, we assigned positive and negative anomalies of 2% alternately to the unknown parameters (ΔS, ΔA, and ΔB) at the 3-D grid nodes. The input anomalies are superposed on the starting 1-D model as shown in Figure 3 to construct a synthetic 3-D checkerboard model, in which the topographies of the three discontinuities are also included. According to equations (2) and (3), the values of +2% for both A and B indicate an input P wave azimuthal anisotropy of ($\alpha_0 = 2.83\%$, $\psi_0 = 112.5°$), while −2% leads to ($\alpha_0 = 2.83\%$, $\psi_0 = 22.5°$). We then calculated synthetic travel times for the input (3-D) checkerboard model and inverted them. The distribution of seismic stations and events in the synthetic data set is the same as that of the real data. Random noise with a standard deviation of 0.1 s was added to the synthetic data to simulate the picking errors of the P wave arrival-time data.

Figures 5 and 6 show the recovered model for the isotropic P wave velocity anomalies (ΔS or ΔV) and P wave azimuthal anisotropy, respectively. They show similar patterns of spatial resolution, following the ray coverage (Figure 4). We define a single parameter to describe the recovery rates of both amplitude and FVD of azimuthal anisotropy (following Huang, Zhao, et al., 2015):

$$R_{AA} = \left| \frac{\alpha}{\alpha_0} \cdot \cos(\varphi - \varphi_0) \right| \tag{6}$$

This parameter equals to one if the input anisotropy is completely recovered, while it approaches zero if the input anisotropy is poorly recovered. We selected $R_{AA} = 0.2$ as the threshold value above, which the azimuthal anisotropy is considered resolved according to the CRT results (Figure 6). Note that it is only an approximate and relative measure of the reliability of the obtained anisotropy. In the crust (10- and 25-km depths) the input models are better recovered in the northern region (Iquique) than those in the southern part (Tocopilla). At 40- and 60-km depths, the input model is recovered well above the subducting slab. At 80- and 100-km depths, only the region close to the upper boundary of the slab is recovered. Overall, the isotropic anomalies are recovered better than the anisotropic structure because the anisotropic inversion requires very good ray azimuthal coverage (Huang, Zhao, et al., 2015).

Further recovery tests for the actually revealed structures are also carried out, which are discussed in section 3.3 after describing the results obtained by the inversion of the real data.
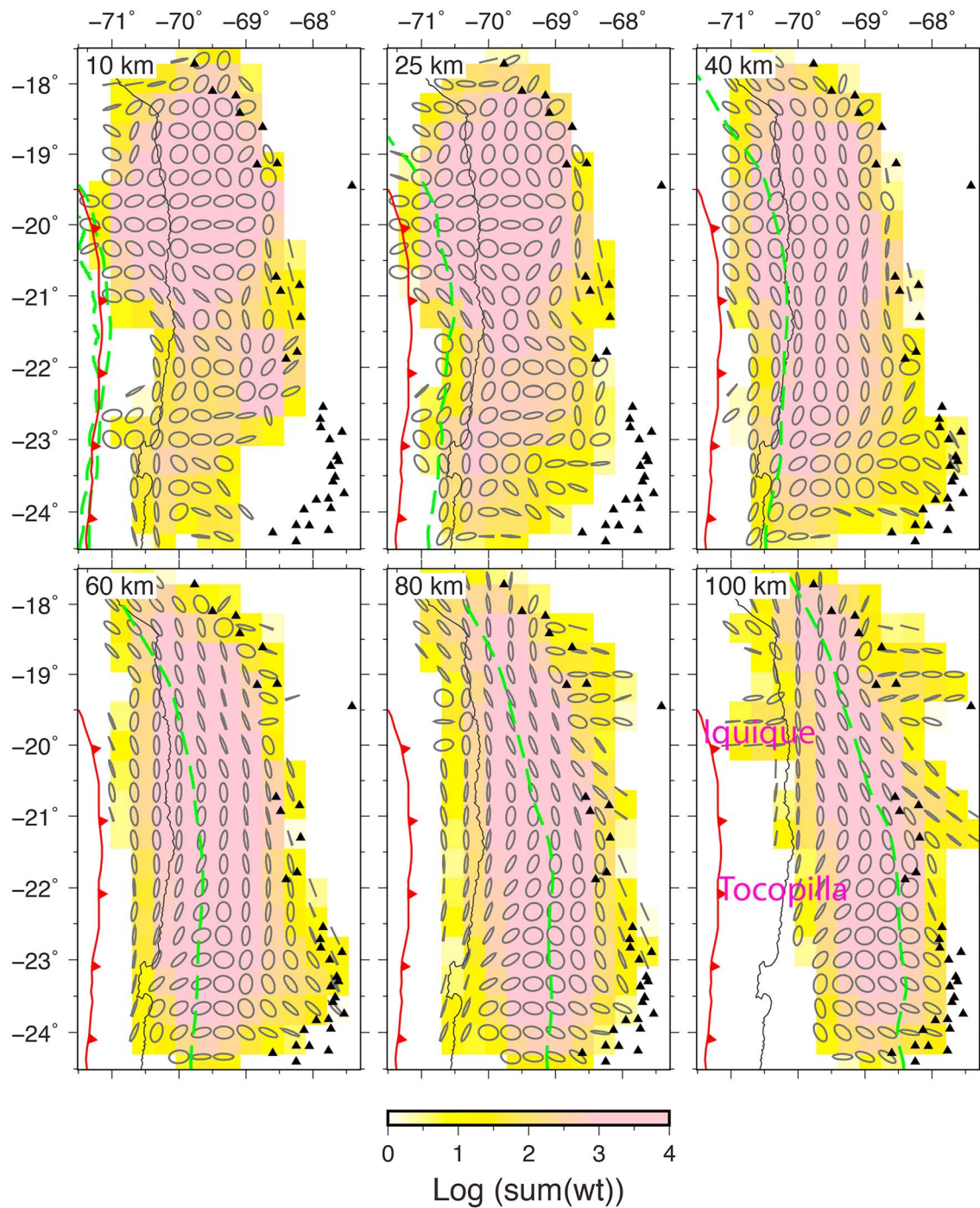
Figure 4. Density of ray paths. The yellow ellipses indicate the azimuthal coverage of the sub-horizontal rays (see text for details). The red and green lines show the trench and the upper boundary of the slab at the corresponding depth, respectively. The black triangles show the active volcanoes.

3.2. Seismic Velocity Anomalies and Anisotropy

We chose the third iteration result as the preferred model because the reduction of the root-mean-square (RMS) traveltime residual becomes insignificant after further iterations (Figure S1). Figures 7–9 show the 3-D Vp structures including azimuthal anisotropy in the study region. The RMS traveltime residual is reduced from 0.269 s to 0.214 s. We also performed an isotropic inversion that only solves for isotropic Vp structure (Figures S2–S4; the final RMS residual is 0.219 s) and one more anisotropic inversion with a
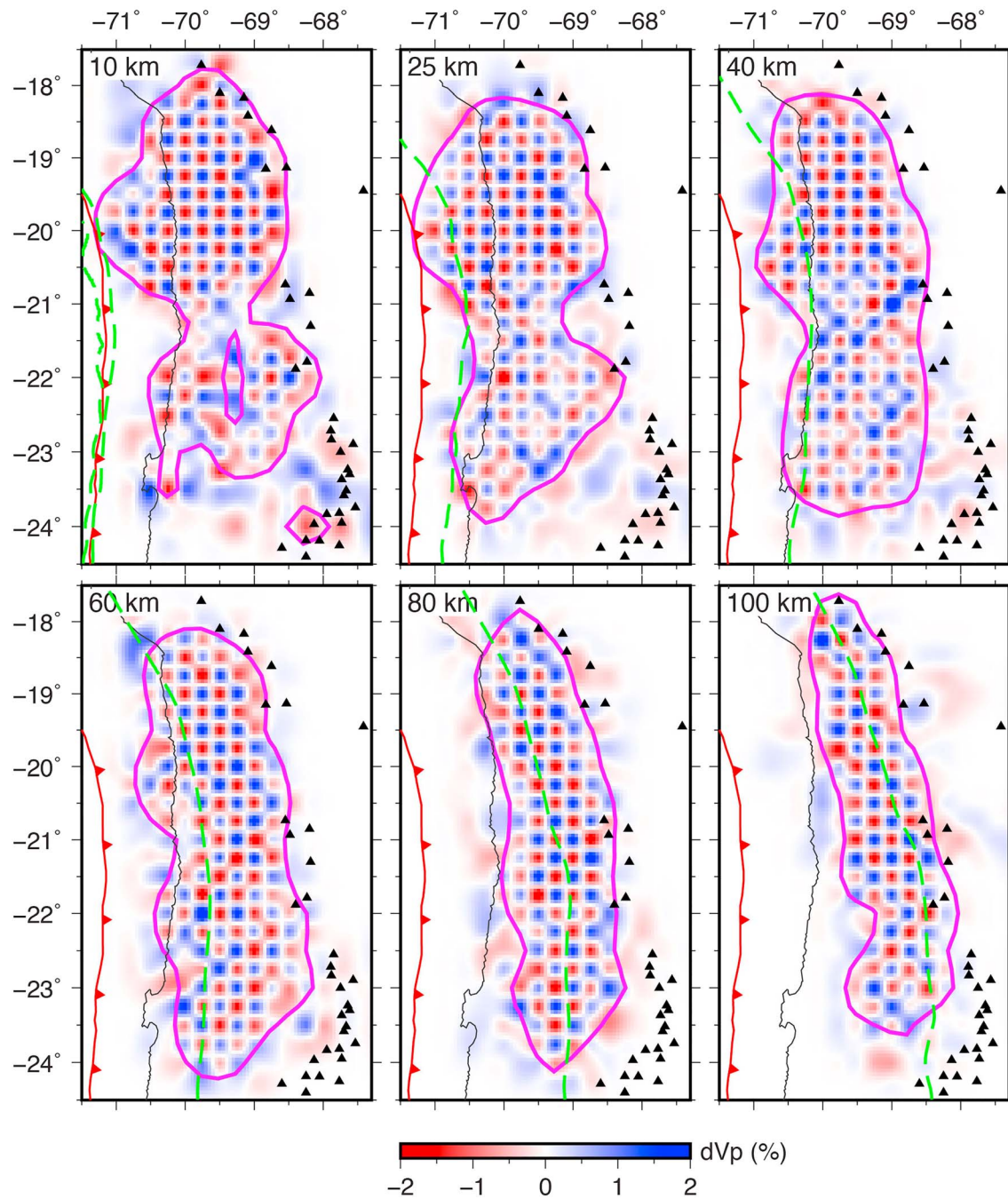
Figure 5. Isotropic anomalies recovered for an anisotropic checkerboard resolution test. The bold magenta lines outline the regions that have a good resolution. For the other labeling, see Figure 4.

starting model that does not contain a high-velocity subducting slab (Figures S5–S7; the RMS residual is reduced from 0.272 s to 0.209 s). The differences of *P* wave azimuthal anisotropies inverted with (Figures 7–9) and without (Figures S5–S7) the initial high-velocity slab are small in the shallow part (Table S2); the differences in the anisotropy amplitude and FVD are on average 0.30% and 20°, respectively. The differences become larger in the deeper parts of the model and reach 0.53% and 40°, respectively. The Vp model including azimuthal anisotropy explains the data better than the isotropic Vp model. However, introduction of the high-velocity slab into the starting model increases the data misfit, which may indicate that the prior assumption of uniformly higher-velocity in the subducting slab is not
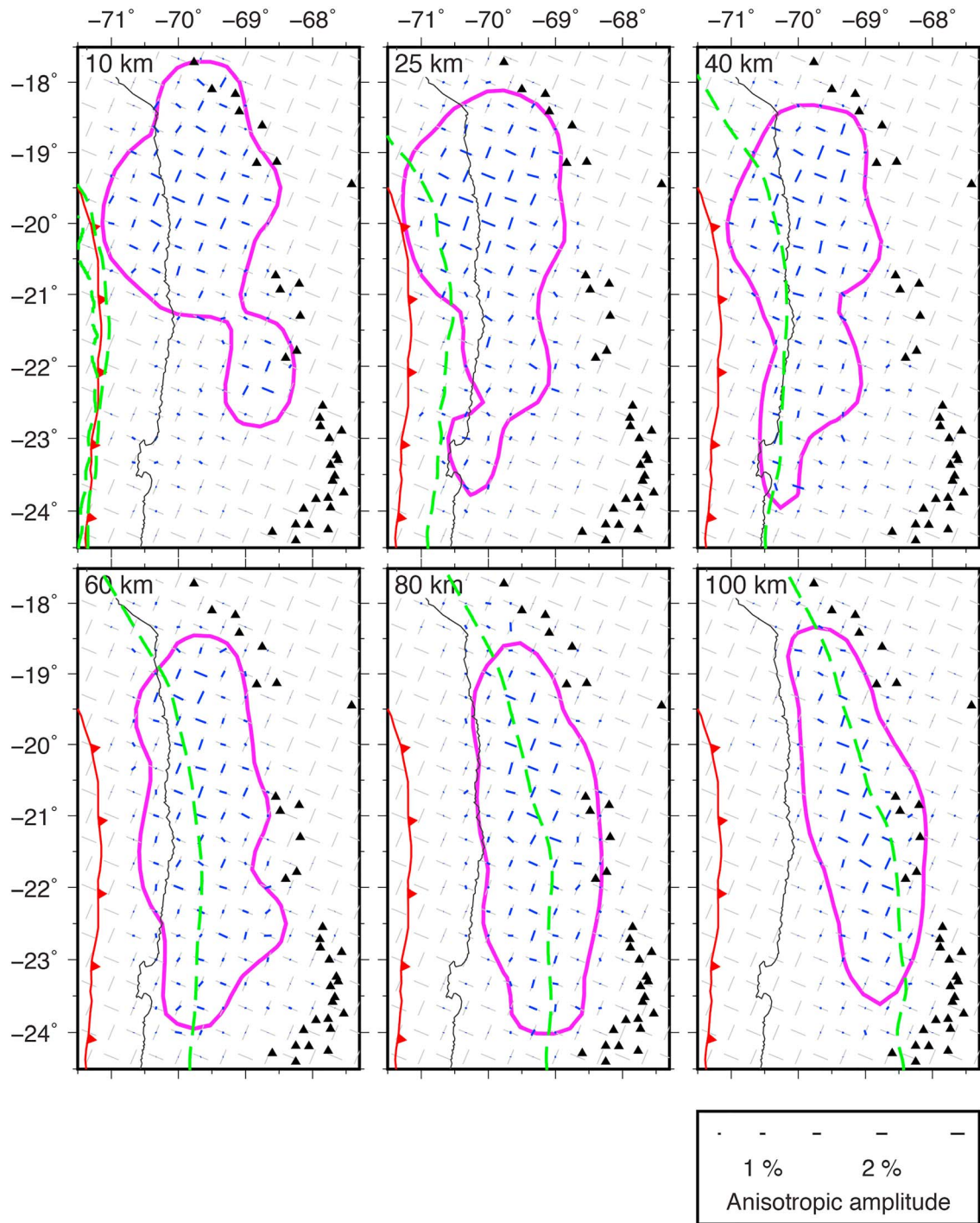
Figure 6. *P* wave anisotropy recovered by a CRT (blue bars). The orientation and length of the short bars denote the fast velocity directions and anisotropic amplitudes of *P* wave azimuthal anisotropy, respectively. The gray bars denote the input model. The bold magenta lines outline the regions where the input anisotropy is well recovered. For the other labeling, see Figure 4. Note that the well-recovered region is somewhat smaller than that for the isotropic anomalies shown in Figure 5.

optimal. Nevertheless, we prefer this model because it is expected to yield more accurate theoretical travel times and ray paths, as mentioned above. We also carried out an inversion assuming a flat intracrustal discontinuity at 20-km depth and a flat Moho at 35-km depth in the starting model to investigate the influence of the discontinuity topography (Figures S8–S10; the final RMS residual is 0.220 s). This

Azimuthal anisotropy
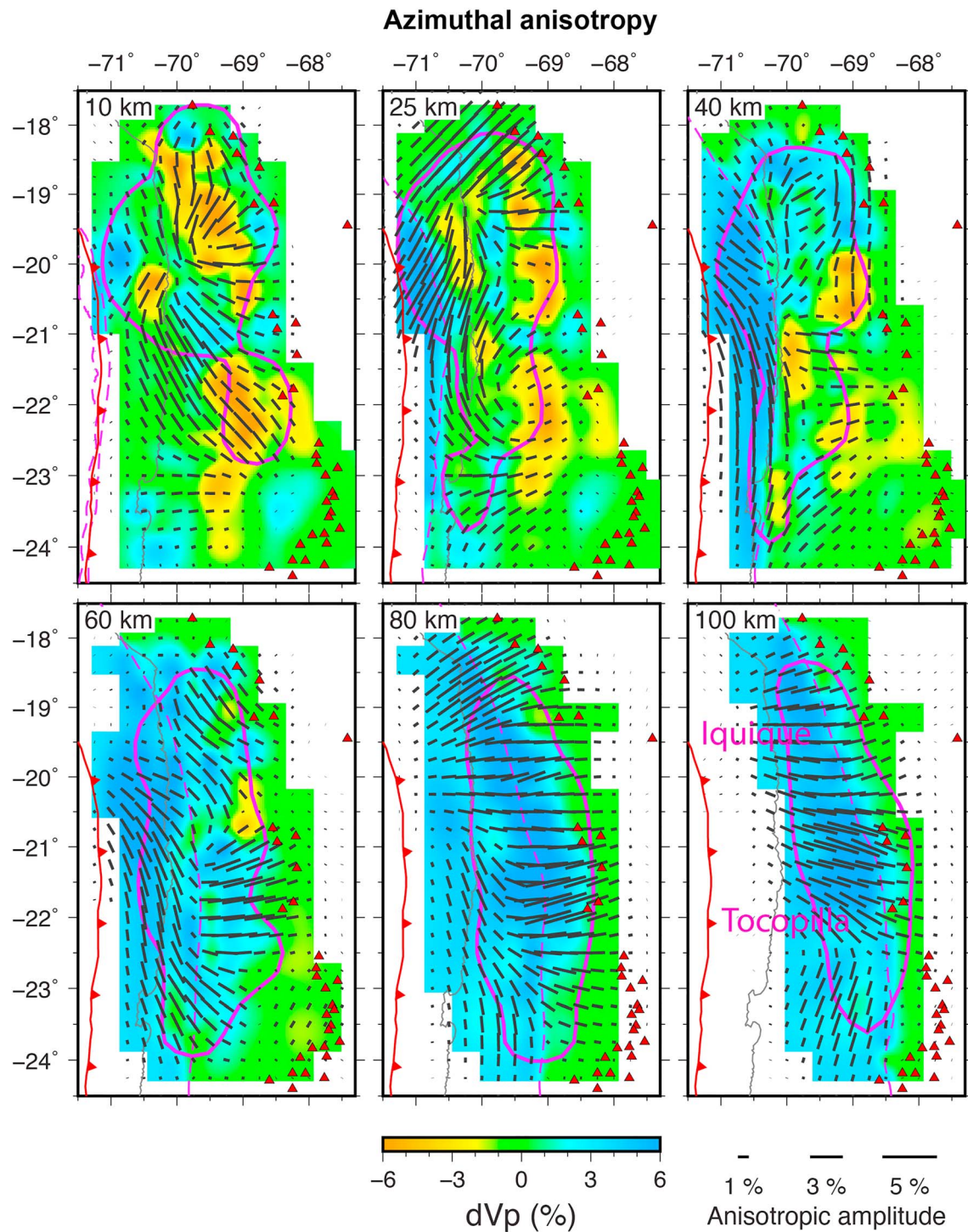
Figure 7. *P* wave velocity anomalies (background colors) and azimuthal anisotropy (short bars) obtained by the tomographic inversion. The magenta lines outline regions with good recovery of both isotropic velocity perturbations and azimuthal anisotropy. For description of anisotropy visualization and other labeling, see Figures 4–6.

inversion yields a larger RMS residual than that of the inversion with undulating discontinuities in the starting model. The differences of *P* wave anisotropies are significant but did not change the first-order patterns (Table S2). The differences in the anisotropy amplitude are generally larger than 0.4% with a maximum value of 0.72% at 60-km depth; the differences in the FVD are larger than 30° at many grid nodes.
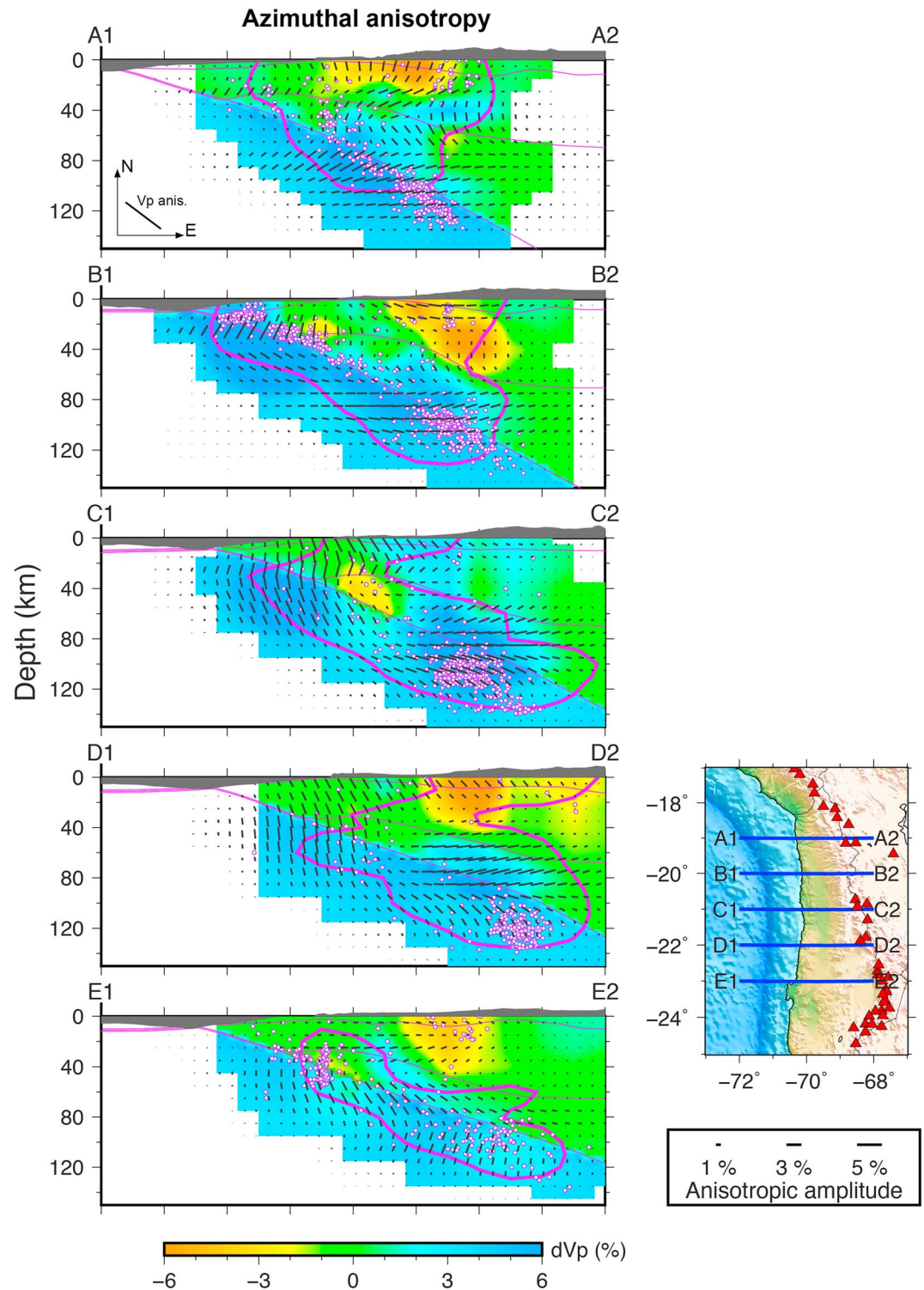
Figure 8. *P* wave velocity anomalies and azimuthal anisotropy along five E-W vertical cross-sections (shown in the bottom-right inset). Note that the short bars show the *P* wave FVDs in the horizontal plane, that is, with vertical standing for N-S and horizontal for E-W directions. The bold magenta lines outline the regions where the input anisotropy is well recovered, as shown in Figures 6 and 7. The three thin magenta lines denote the intracrustal discontinuity, the Moho, and the upper boundary of the slab, respectively (Tassara & Echaurren, 2012). The white dots denote earthquakes occurring within a 5-km width of each profile.
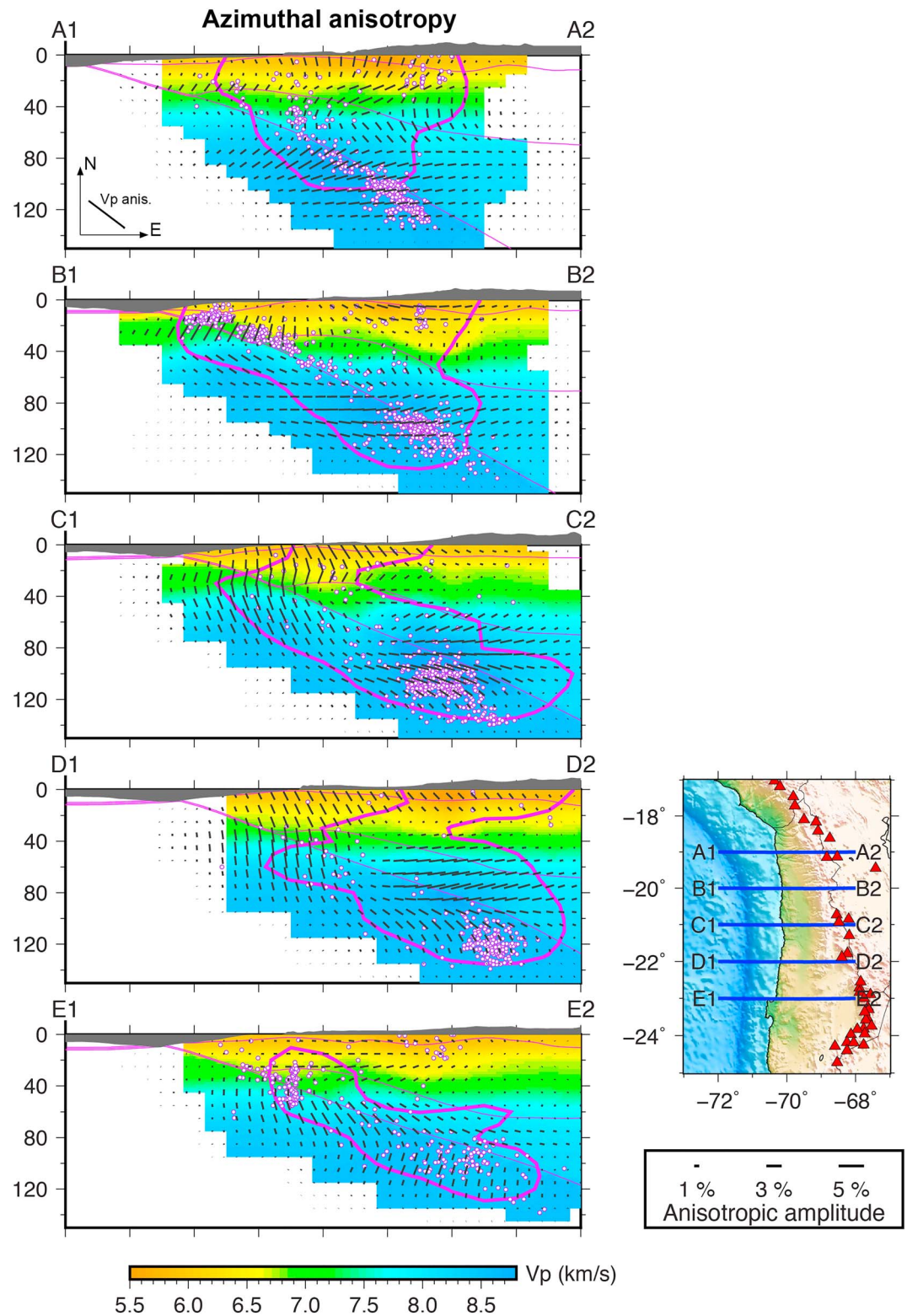
Figure 9. The same as Figure 8 but showing absolute *P* velocities instead of Vp perturbations.

The imaged first-order features (especially the *P* wave azimuthal anisotropy) are similar in all these variants in the areas where the CRT test indicates a good resolution. The isotropic Vp images also preserve the dominant patterns revealed by Comte et al. (2016). For example, in the supraslab mantle, there is an obvious
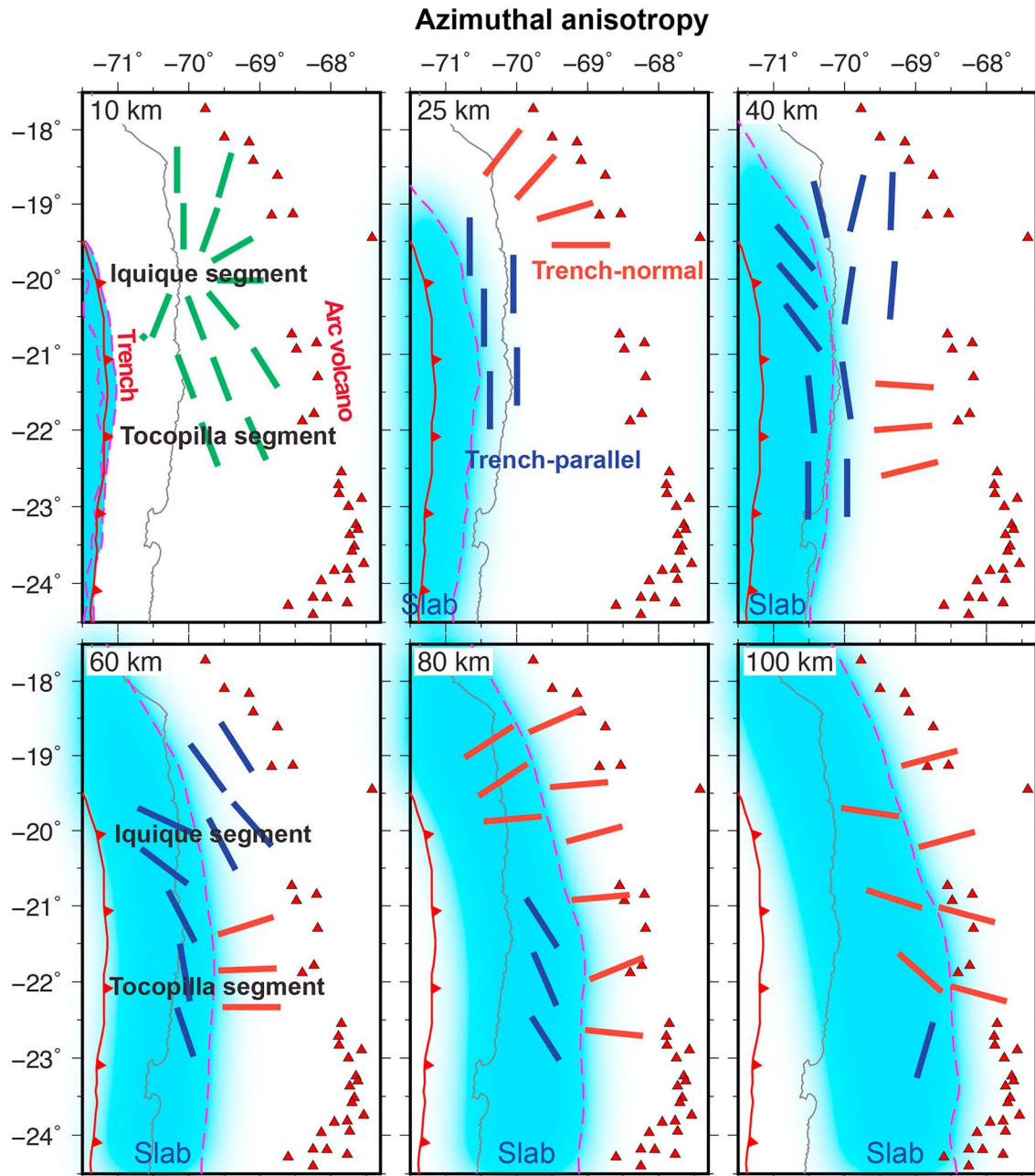
Figure 10. Simplified features of *P* wave azimuthal anisotropy in northern Chile. The short bars denote orientations of azimuthal anisotropy at different depths. The blue bars show the FVDs that are subparallel or oblique with small angles to the trench (named trench parallel for short); the red bars show the FVDs that are subnormal or oblique with large angles to the trench (named trench normal for short). The blue regions mark the subducting slab. For the other labeling, see Figure 7.

transition from relatively lower velocities at 40- to 80-km depths to higher velocities at 80- to 120-km depths, although the extent of the anomalies differs somewhat. The high velocities in the subducting slab are revealed by the inversion even though they are not present in the starting model. Unsurprisingly, due to the different prior information and poor data constraints on the deep parts of the high velocity slab, it seems to be imaged quite differently by the different inversions.

The pattern of *P* wave azimuthal anisotropy changes drastically with depth (Figure 7). Figure 10 shows simplified features of the *P* wave azimuthal anisotropy at different depths. At 10-km depth, FVDs appear to
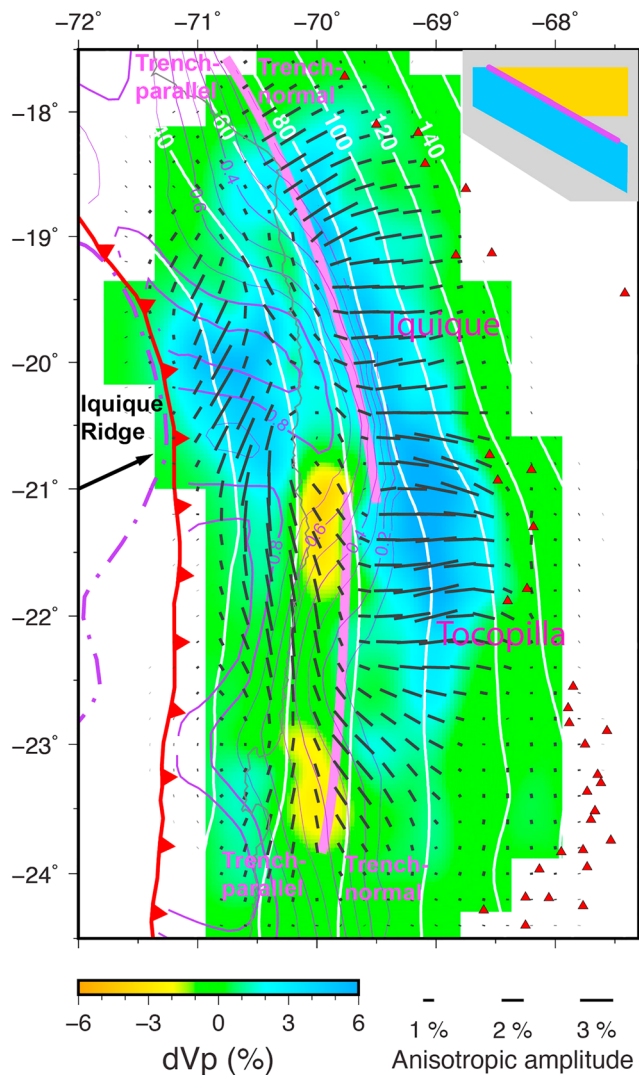
Figure 11. *P* wave velocities and anisotropy sampled along the plate interface (a curved plane right above the slab) as shown in the top-right inset. The white contour lines denote the upper boundary of the slab. The purple contour lines show the interplate-locking degree along the plate interface (Li et al., 2015). For the other labeling, see Figures 1 and 7.

radiate from near Iquique (around 20°S, 70°W). At 25-km depth, the radiating pattern is still visible, but its center is displaced by nearly 100 km to the north. However, the nearly N-S oriented FVDs along the coast are the predominant feature at this depth. At 40- and 60-km depths, the FVDs above the slab change from dominantly trench-parallel or oblique with small angles (N-S to NW-SE) in the Iquique segment to trench-normal or oblique with large angles (EW to ENE-WSW) in the Tocopilla segment, while the FVDs in the subducting slab are generally trench parallel. At 80- and 100-km depths, the FVDs are NE-SW in both the slab and mantle wedge in the Iquique segment. In contrast, they change from trench parallel in the slab to trench normal in the mantle wedge in the Tocopilla segment (Figure 10).

Another way to describe this feature is to note that the FVDs right above the subducting slab change from nearly N-S in the shallow parts to E-W in the deep parts (Figure 11). The change occurs around 60- to 80-km depths in the Iquique segment (18°S–21°S) but shallower, around 40- to 60-km depths in the Tocopilla segment (21°S–23°S; Figures 8 and 9).

3.3. Restoring Resolution Tests

We conducted another suite of synthetic tests, so-called restoring resolution tests (RRT), to further evaluate the reliability of the recovered Vp anomalies and azimuthal anisotropy. The RRT is similar to the CRT except that the input model is manually constructed based on the obtained tomographic images. The RRT can be also used to investigate the trade-off between the isotropic and anisotropic structures due to insufficient ray azimuthal coverage in some areas (Figure 4). We first take the isotropic features of our *P* wave anisotropic model (Figure 7) as input model and generate the synthetic data set. The isotropic features are mostly recovered (Figure S11). However, there are notable artifacts in the anisotropic model in which anisotropy should not exist if the recovery is perfect. The maximum amplitude of anisotropy (the artifacts) reaches 1%, approximately one third of the regional average of the azimuthal anisotropy. Along 21°S at 40- and 60-km depths, the FVDs are comparable to the actual inversion (Figure 7) to some degree but with a smaller amplitude. Another test (Figure S12) is conducted to examine the opposite effect by taking only the anisotropic features of the *P* wave anisotropic model (Figure 7) as the input model. The smearing from anisotropic to isotropic features is very weak and only notable in very limited areas. These tests thus indicate that the isotropic and anisotropic features can generally be distinguished. Although some trade-off between isotropic and anisotropic structure occurs, it does not impact the first order patterns described above.

Next we focus on the following two structures with an input model containing both isotropic and anisotropic structures: (1) the radiating FVDs in the crust (Figures 10 and S13a) and (2) the transition from high velocity with N-S FVDs in the Iquique segment to low velocity with E-W FVDs in the Tocopilla segment in the mantle wedge (Figures 10 and S13d). The RRT results confirm that the data are able to reveal these velocity and anisotropy features to the west of the volcanic arc, although both anomalies and anisotropy amplitudes are reduced by ~20%–30% (Figure S13).

The final set of RRT tests are performed to investigate vertical smearing of the anisotropy above and within the subducting slab. All the input models of the tests have no isotropic Vp anomalies; anisotropic structure is confined to two 10-km thick dipping layers following the slab contours. The shallower layer is placed directly above the slab, and the deeper layer is embedded within the slab, with both layers being separated by 10 km. Also, all the input models have the same top layer anisotropic structure, which includes the transition from NNW-SSE FVDs near the trench to ENE-WSW FVDs beneath the magmatic arc at a depth of 60 km of the
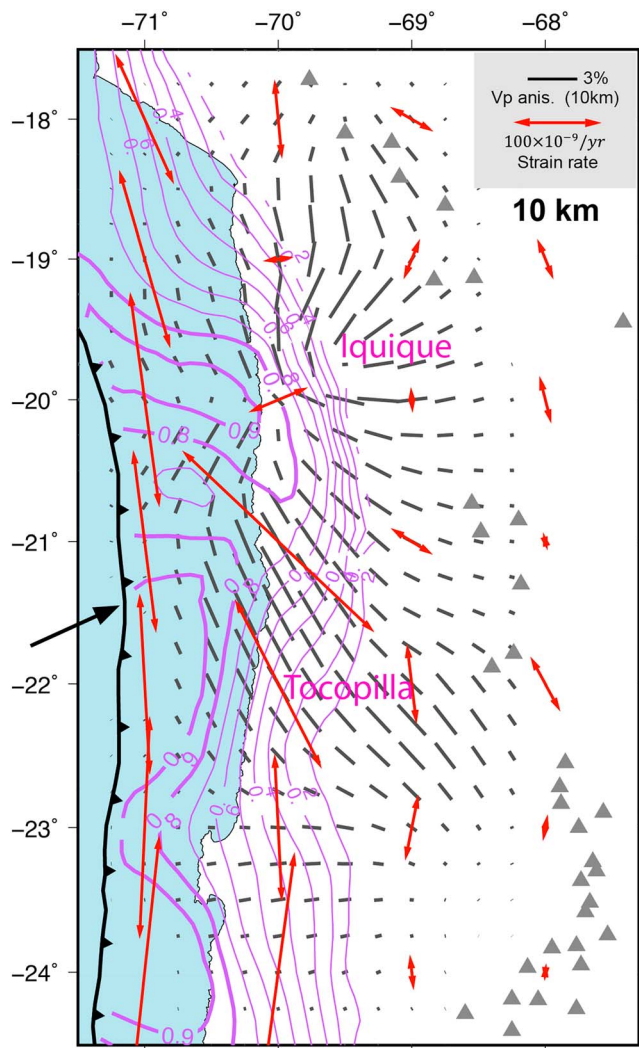
Figure 12. Comparison of the *P* wave anisotropy at 10-km depth (black bars) with the strain field (double-headed red arrows) inverted from GPS observations in northern Chile (Kreemer et al., 2014). The purple contour lines show the interplate-locking degrees along the plate interface (Li et al., 2015); bold lines denote the highly locked areas with a locking degree greater than 0.8. For the other labeling, see Figure 1.

slab interface (Figures 11 and S14–S16). The input structure in the slab is different for each RRT: the first model has NNW-SSE FVDs at slab interface depths below 60 km (i.e., when the top of the lower anisotropic layer is at less than 70-km depth; Figure S14). The second model is the same, except that ENE-WSW FVDs are found in the deeper slab (Figure S15). In the third model the slab is isotropic (Figure S16). No significant cross talk to isotropic structure is discernible. All the three tests clearly resolve the transition of the FVDs above the slab, suggesting that it is a robust feature. The input structure in the slab is also well recovered. There are notable smearing effects near the trench (Figures S14d–S16d) and beneath the active volcanoes (Figure S14b), but anisotropy amplitudes are much smaller than in the areas where anisotropy is present in the input model. These RRT results show that the anisotropic structures above and in the subducting slab can be resolved independently, without strong vertical smearing.

4. Discussion

The isotropic velocities obtained in this study, both from isotropic and anisotropic inversions, show dominant first-order features as revealed by the previous study (Comte et al., 2016). We did not reveal strong velocity anomalies beneath the active volcanoes as in other subduction zones (e.g., Huang et al., 2011, Wang & Zhao, 2008, Zhao et al., 1992) because the present data set does not cover the volcanic areas. We imaged the high-velocity slab even when it was not contained in the initial velocity model, albeit only patchily as determined by the ray coverage (Figures S5–S7). More importantly, we found a transition from lower to higher velocity along the top of the slab (Figures 8 and 9), which may reflect the basalt-to-eclogite conversion in the subducting crust (Bloch et al., 2014; Comte et al., 2016). These features have been comprehensively discussed in these previous works; hence, we will not discuss them here. Instead, we focus on the anisotropic structures in the northern Chile subduction zone and their tectonic implications.

4.1. Anisotropy in the Overriding Plate

The crustal anisotropy shows FVDs radiating from a point near Iquique (near 20°S, 70°W; Figures 7 and 10, at 10-km depth). In the northern Chile subduction zone, the convergence between the Nazca plate and South America is directed toward the ENE (Figure 1b). The regional crustal strain field in the overriding plate is characterized as nearly N-S trending maximum strain (Figure 12; Kreemer et al., 2014), which is subparallel to the trench. However, onshore this pattern is disrupted in a wide zone along the Iquique segment, with much weaker strain with anomalous E-W trending maximum strain found near Iquique at ~20°S (Figure 12). The strike of the maximum strain rotates from NE-SW in the north (69°W–70°W, 19°S–20°S) to NW-SE in the south (69°W–70°W, 20°S–21°S; Bedford et al., 2015; Kato et al., 2016; Kreemer et al., 2014). The region is located right at the subduction symmetry plane where the Nazca Plate has to deform to accommodate the curved continental margin of the South American Plate (Gephart, 1994). This tectonic feature may induce the surface velocity field to converge toward the symmetry plane (Bevis et al., 2001), which produces the NE-SW and NW-SE interseismic extension directions to the north and south of the symmetry plane, respectively. The extension directions agree with the FVDs of our P wave azimuthal anisotropy. The surface strain field from GPS observations (Kreemer et al., 2014) also shows some consistent features, especially in the region of 20.5°S–22.5°S and 69°W–70°W, where the strengths of both strain field and anisotropy are much larger than those in adjacent regions.

The strain field (weak with NE-SW orientations) between 19°S and 20°S (69°W–70.5°W) is quite different from the regional pattern, and the anomaly may indicate some specific tectonic features in this region. The features seem to be related to the distribution of interplate locking along the plate interface. A notably deeper extending (to a depth of 60 km or greater), highly locked (with a locking degree >0.8) asperity has been inferred near Iquique (Figure 1b; Li et al., 2015; Métois et al., 2016; Ortega-Culaciati et al., 2015). This asperity appears to be isolated from other asperities and acts as a point-like source. Sandbox experiments (Dominguez et al., 1998) show that a subducting seamount generates radiating maximum compressive stress and a series of backthrusts landward in the overriding plate. Many strike-slip faults also develop in a radiating pattern from the point source. It should be noted that SPO produced by the frontier backthrusts would produce circular FVDs around the seamount. If the SPO pattern is reorganized by the strike-slip faults or is overprinted by aligned cracks newly formed due to continuing radiating maximum compressive stress, the observed radiating FVDs in the upper crust might result (at 10-km depth in Figures 7 and 10). However, the coseismic strain field modeled for the 2010 Maule earthquake (Mw 8.8), Chile, in a similar tectonic location as the Iquique earthquake, shows different orientations (Aron et al., 2013): the extension directions show a dominant radiating pattern, thus a circular pattern results for the shortening directions, which would predict circular FVDs for crustal SPO from crack formation. But the radiating FVDs obtained in our model at 10-km depth may also reflect the anisotropy due to mineral preferred orientations in the deeper crust. The crustal events used in this study usually occurred deeper than 10 km (Figure 2), but the upper-crustal layer susceptible to crack-induced anisotropy is expected to be less than 10 km (Figure 3e). Many rays travel in the mid and lower crust and sample the anisotropic structures there. The *P* wave anisotropies imaged at 10-km depth therefore are likely to be also significantly affected by the deeper crustal structures. The mineral fabrics in the deeper crust are expected to produce FVDs parallel to the extension direction from CPO, that is, a radiating pattern as we imaged (Figures 7 and 10). Nevertheless, we can hardly confirm a confident model for the radiating FVDs in this study. Further analysis and observations are necessary to better understand the geological processes.

In the lower crust and upper mantle (40- and 60-km depths), ductile deformation dominates instead, implying CPO, which generally results in FVDs normal to the maximum stress. This mechanism thus represents a plausible interpretation for the observed FVDs (NW-SE at 60 km, 18°S–21°S) normal to the subduction direction. Another candidate is B-type olivine, which is discussed in the following.

The anisotropy in the overriding plate of the Tocopilla segment (21°S–23°S) is not clear. Our synthetic tests indicate that the anisotropy there has a lower resolution (Figure 6). In the lower crust (25-km depth) and uppermost mantle (40-km depth; Figure 7), the structures there may be affected by mantle-wedge flow or interplate deformation, as discussed below.

4.2. Anisotropy in the Mantle Wedge

The structure in the mantle wedge close to the active volcanoes in the Western Cordillera (Figure 1c) is not well resolved in the present study because most events and all stations are located under the forearc region (Figure 2). However, some first-order features are robust. The dominant feature are the trench-normal FVDs, especially in the Tocopilla segment (21°S–23°S; Figures 7 and 8). Trench-normal anisotropy has also been observed in the northeastern Japan subduction zone (Huang et al., 2011; Ishise & Oda, 2005; Liu & Zhao, 2016; Wang & Zhao, 2008), which may be caused by the mineral fabrics (e.g., C- or E-type olivine) developed in the mantle wedge in response to corner flow induced by active subduction (Figure 13; Huang et al., 2011; Karato et al., 2008; Wang & Zhao, 2008).

In contrast, trench-parallel FVDs accompanying high velocities are found at 40- to 60-km depths in the Iquique segment (18°S–21°S; Figures 7 and 10). As the interplate locking in the Iquique segment extends downward to ~60-km depth, the overriding lithosphere at this depth is under ENE-WSW compression (Figure 13a). The trench-parallel anisotropy (with N-S to NW-SE FVDs) could be produced in response to ductile deformation induced by this stress field. On the other hand, B-type olivine fabric may have developed in the forearc mantle wedge. The subducting Nazca plate is older in the Iquique segment (Mueller et al., 2008); the Iquique Ridge is also located there (Figure 1a). Therefore, the subducted plate beneath the Iquique region may be relatively colder and contain more fluids than the adjacent segments (Bloch et al., 2014; Comte et al., 2016). The deeply extending high interplate locking may induce higher stress in the
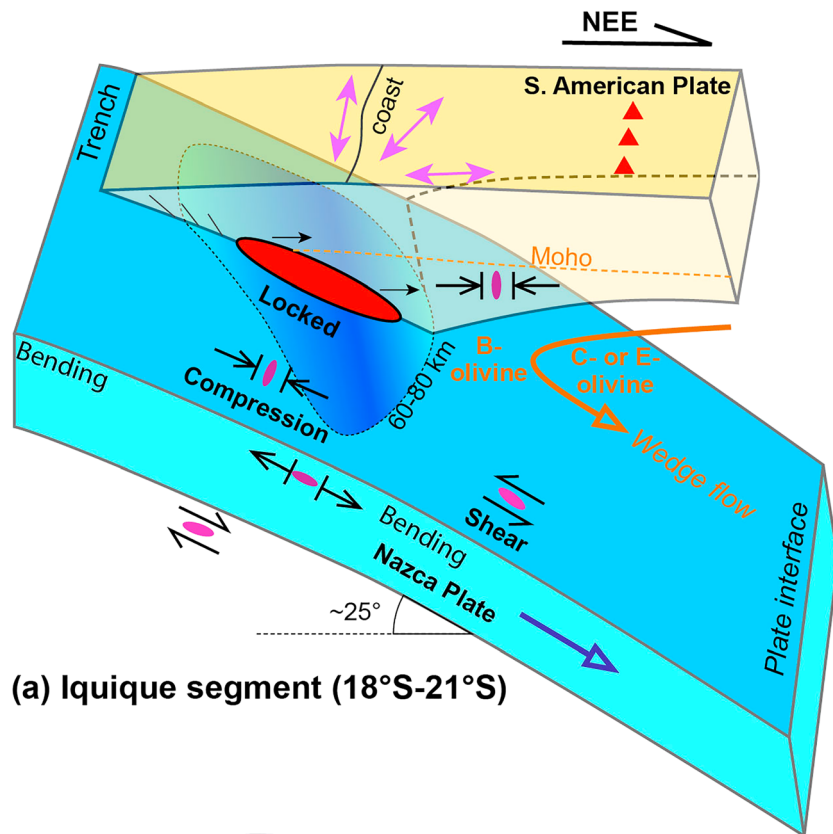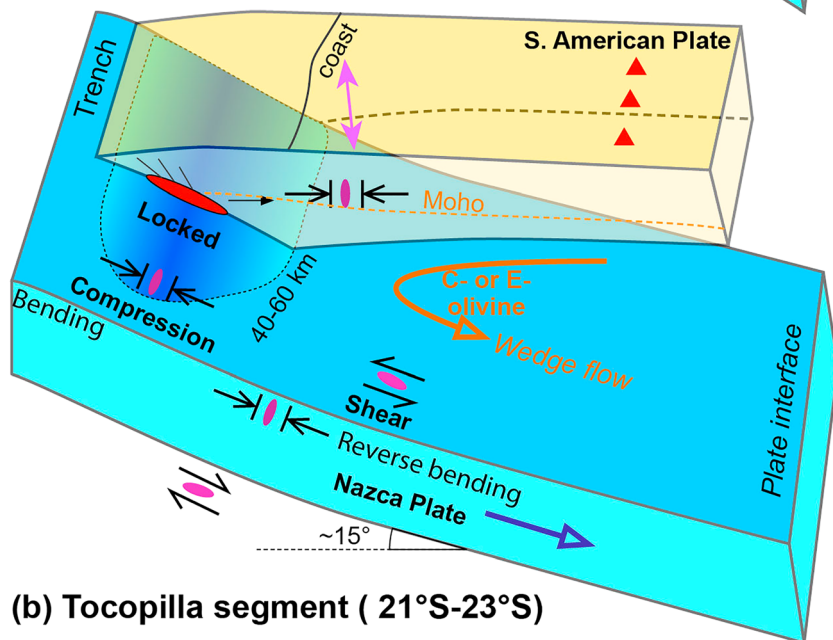
Figure 13. Two conceptual models (not to scale) illustrating a plausible deformation pattern in the northern (Iquique) and southern (Tocopilla) segments of the northern Chile subduction zone, which could explain some of the features of the observed anisotropy. The yellow and blue colors denote the overriding and subducting plates, respectively. Deep blue colors indicate significant interplate locking along the plate interface, with red ellipses showing the highly locked asperities. The magenta ellipses with coupled arrows imply the deformation patterns in different layers of the subduction zone. The double-headed magenta arrows denote the maximum extension produced at surface.

neighboring mantle wedge. Therefore, B-type olivine fabrics are likely to exist in the forearc mantle wedge, which could also explain the trench-parallel anisotropy (Karato et al., 2008; Kneller et al., 2005).

4.3. Anisotropy in the Subducting Slab

We only used local events in this study, and the intermediate-depth earthquakes only occurred in the upper part of the subducting slab. Hence, the ray paths do not pass through the lower part of the slab. The anisotropy we obtained only reflects the structure of the upper part of the subducting slab. In northern Chile, the geometry and structures of the subducting slab in the southern (Tocopilla) and northern (Iquique) segments are different. The southern segment is characterized by low-angle (~15°; Figure 3d) subduction of a relatively younger slab (Figure 1a). In contrast, in the northern segment, the subducting slab is older (Figure 1a) and its dip angle is larger (~25°; Figure 3b), producing trench-normal (~E-W) extension in the upper part of the subducting slab (Figure 13a). Otherwise, the Iquique Ridge is subducting under Iquique in northern Chile (Figure 1a). The character and strength of the slab here are therefore different from those in adjacent regions, and so deformation within the slab may be affected significantly. The FVDs in the subducting slab exhibit notable along-arc variations: they are generally trench parallel (Figures 7 and 10, at 40- to 80-km depths) in the Tocopilla segment while trench-normal in the Iquique segment (Figures 7 and 10, at 80- and 100-km depths). The anisotropy in the slab may arise from either the fossil fabric formed during plate formation at a mid-oceanic ridge or from the active deformation accompanying subduction (Eakin et al., 2015; Liu & Zhao, 2017; Plomerová & Babuška, 2010; Wang & Zhao, 2008). Fossil anisotropy would predict FVDs normal to seafloor magnetic stripes, that is, FVDs subparallel to ENE-WSW in northern Chile (Figure 1a; Mueller et al., 2008). This pattern is indeed observed in the Iquique segment. But in the Tocopilla segment, the *P* wave anisotropy in the slab has NNW-SSE FVDs (Figures 7 and 10), which suggests that the observed anisotropy at least in the south is mainly caused by present deformation (Eakin et al., 2015; Faccenda et al., 2008) rather than fossil anisotropy.

The oceanic slab experiences bending near the trench and subsequent unbending (even reverse bending) as it subducts. Accordingly, the upper part of the slab is under extension and compression in sequence (Gamage et al., 2009). Under the extension in the shallow outer rise during slab bending, many trench-parallel faults are formed in the upper part of the slab, through which abundant water enters the slab. As the depth and temperature increase, the hydrated slab tends to be serpentinized in sheet-like structures below major outer rise faults, which could produce trench-parallel SPO anisotropy (Faccenda et al., 2008). However, we obtained dominant trench-normal anisotropy in the northern Iquique segment (Figures 7 and 10, at 80- and 100-km depths), which contradicts this hypothesis. Here we must be aware of the lower resolution of our tomography in this area, although the synthetic tests indicate that larger features can be recovered in general. On the other hand, slab bending can also be expected to directly affect anisotropy through strain-induced CPO: the trench-normal extension produced by bending in the upper part of the slab would lead to trench-normal alignment of the fast axis when it occurs mostly under ductile deformation conditions at depth (Figure 13a; Karato et al., 2008). The two possible origins of slab anisotropy induced by subduction processes, mineral fabrics and aligned faults, thus predict perpendicular directions. In the Tocopilla segment, the slab bending is weak, so the trench-parallel anisotropy due to the aligned faults is dominant (Faccenda et al., 2008). In the Iquique segment, the slab bending is strong and continues to at least 150-km depth, that is, probably placing the uppermost parts of the slab in the ductile regime, promoting the formation of strong mineral fabrics and trench-normal slab anisotropy. However, there is an argument whether the slab bending or unbending produces sufficient strain for mineral Lattice Preferred Orientation (LPO) in the upper part of the slab (e.g., Kaminski & Ribe, 2002).

An alternative hypothesis (or at least a contributing factor) may relate to subduction of the Iquique Ridge. The orientations of the cracks or faults developed during the slab bending may be affected by the ridge, and in particular be less organized, that is, less likely to give rise to a well-developed SPO anisotropy.

4.4. Anisotropy Along the Plate Interface

Along the upper boundary of the subducting slab is the megathrust zone where the subducting and overriding plates are interacting. Figure 11 shows Vp anomalies and azimuthal anisotropy along the plate interface, while Figure S17 shows the inversion result obtained with a starting Vp model that does not include a high-velocity slab. We used many offshore aftershocks of the 2014 Iquique earthquake whose depths are less well

constrained. Therefore, we carried out one more inversion as a further check, by adding random Gaussian noise with a standard deviation of 5 km to the focal depths of the suboceanic earthquakes after relocation. The inversion result shows that the focal depth errors of ~5 km do not cause notable variations to the recovered isotropic and anisotropic structures (Figure S18).

Toward the east, the dominant *P* wave anisotropy changes from dominantly N-S (trench parallel or oblique) to trench normal. The change occurs at 40- to 60-km depths in the southern segment, and at 60- to 80-km depths in the northern segment (Figure 11). More importantly, the trench parallel or oblique anisotropy is mostly located in regions of significant interplate locking (Li et al., 2015). In contrast, the trench normal anisotropy is dominant where the interacting plates are decoupled.

In the highly locked regions, there is no or very slow motion along the subduction channel during the interseismic cycle (Li et al., 2015; Métois et al., 2016). Horizontal or inclined compression tends to dominate there; either SPO in the shallow accretionary wedge or mineral CPO in the deep part will result in the trench-parallel azimuthal anisotropy (Tommasi et al., 1999). Alternatively, B-type olivine may develop in the forearc mantle, given the high stress and abundant water content in the northern Chile subduction zone, as discussed above (Karato et al., 2008; Kneller et al., 2005). However, the rupture of the 2014 Iquique earthquake may induce simple-shear deformation along the plate interface and may break the CPO or SPO fabrics and affect the anisotropy there, similar to what happened in the NE Japan subduction channel induced by the great 2011 Tohoku-oki earthquake (Mw 9.0; Liu & Zhao, 2017). It may be possible to study the stress and strain accumulation along the plate interface in the coseismic and interseismic cycles with seismic anisotropy. However, the present data set in northern Chile does not have sufficient temporal coverage to reveal the change of Vp anisotropy before, during, and after the great earthquake.

In the deeper part of the subduction zone, that is, below the seismogenic zone and potentially other manifestations of brittle behavior, the subducting slab drives continuous simple-shear deformation at the base of the mantle wedge (e.g., Liu & Zhao, 2017). The typical CPO of C- or E-type olivine could produce the observed trench-normal (also subduction-parallel) azimuthal anisotropy (Karato et al., 2008). The change from trench-parallel (NNW-SSE) to trench-normal (ENE-WSW) anisotropy occurs at 60- to 80 km and 40- to 50-km depths in the northern and southern segment, respectively, which coincides approximately with the lower extent of interplate locking along the megathrust, that is, the transition from brittle behavior to ductile deformation in a convecting mantle (Figure 1b; e.g., Li et al., 2015).

4.5. Implications for Shear-Wave Splitting Measurements

Several studies have used shear-wave splitting to investigate the crustal and upper mantle anisotropy in the northern Chile subduction zone (Figure 14; Bock et al., 1998; Polet et al., 2000; Reiss et al., 2017; Russo & Silver, 1994; Wölbern et al., 2014) with both local *S* waves and core-converted xKS phases (e.g., SKS, SKKS, and PKS). The local *S* wave splitting (Reiss et al., 2017) reflects the anisotropy in the upper part of the subducting slab, and the crust and upper mantle of the overriding plate. The FPD of local *S* wave splitting are mostly trench parallel or trench oblique (Figures 14a and 14b; Reiss et al., 2017). Our Vp anisotropy shows dominant N-S FVDs at 25- to 60-km depths beneath the coastal area (Figures 7 and 10), which correlate with the N-S FPDs of local *S* wave splitting. Note that although the earthquakes mostly occur beneath the active volcanoes, the stations are generally located in the forearc area. Thus, most of the local *S* waves travel through the subducting slab and the overriding lithosphere (Figure 14, inset). The *S* wave splitting measurements mainly reflect the anisotropy in the subducting slab near the hypocenters and the overriding lithosphere near the stations, both of which also show dominant N-S FVDs in our Vp anisotropy.

The FPDs of teleseismic xKS splitting are generally parallel to the motion direction of the Nazca plate (Figure 14c; Long et al., 2016; Reiss et al., 2017). However, the FPDs slightly rotate from ENE-WSW in the south to WNW-ESE in the north. Although our *P* wave anisotropy FVDs also show similar rotation at 60- and 80-km depths, the feature is not notable in other depth ranges. The average amplitude of Vp anisotropy is ~3% in the mantle wedge; the corresponding *S* wave anisotropy is ~4% according to a rough estimate (Sun, 2012). A 30-km thick anisotropic layer in the mantle wedge with an average Vs of 4.4 km/s (Figure 3) can produce an *S* wave splitting delay time of ~0.3 s. Thus, the anisotropy in the mantle wedge could account for at most 30% of the total SKS splitting. In fact, the FPDs revealed by local *S* and SKS splitting measurements are nearly perpendicular to each other. The SKS splitting measurements mostly reflect the
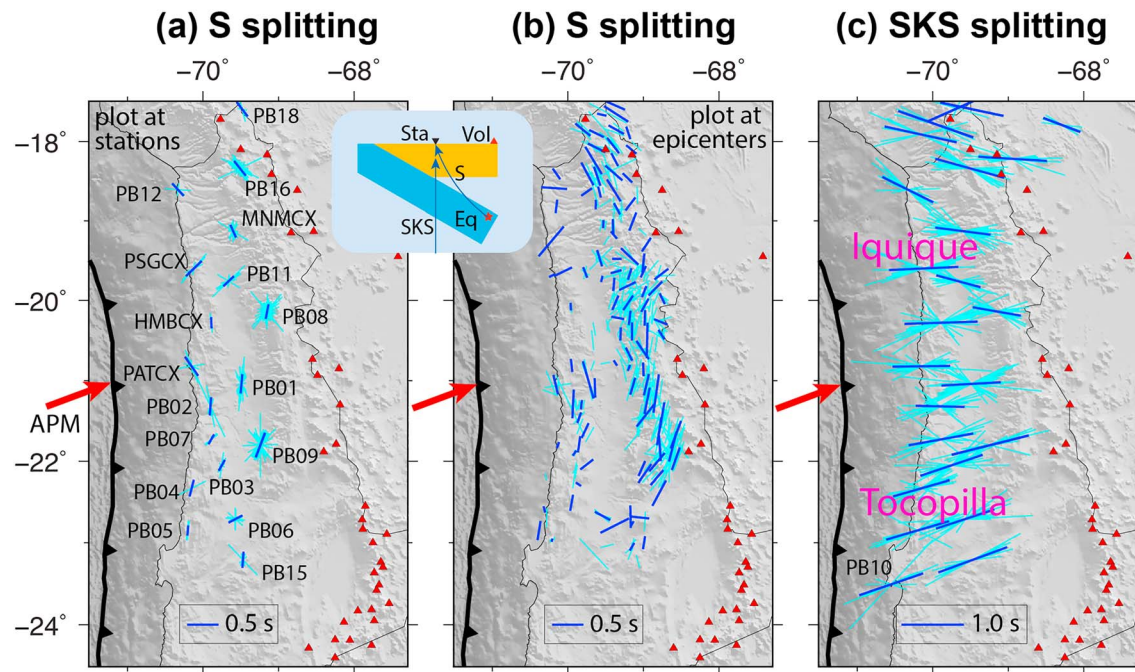
Figure 14. (a) Local *S* wave splitting measurements (Reiss et al., 2017; light blue bars) and the averages (bold blue bars) plotted at station locations. (b) The same as (a) but plotted at epicenters. The averages are calculated at grid nodes for epicenters at less than 10-km distance to the grid node. (c) SKS splitting measurements (light blue bars) and their averages (bold blue bars) plotted at station locations (Long et al., 2016; Reiss et al., 2017). The scales for the delay times are shown in the inset. The red arrows show the convergence direction of the Nazca Plate. The red triangles show the active volcanoes.

anisotropy beneath the subducting slab because the FPDs are subparallel to the plate motion of the Nazca plate. The subducting slab may entrain significant asthenospheric flow right beneath the slab to produce strong mineral fabric and seismic anisotropy (Bock et al., 1998; Hicks et al., 2012; Russo & Silver, 1994). The formation of strong subslab anisotropic fabric has also been simulated by numerical models of plate subduction, whose parameters were chosen to approximate the Nazca plate subduction under South America (Hu et al., 2017).

5. Conclusions

We obtained the first model of 3-D *P* wave azimuthal anisotropy of the northern Chile subduction zone using ~130,000 *P* wave arrival times from 14,695 local earthquakes recorded at 360 stations. Our results reveal different anisotropy patterns in the overriding lithosphere, mantle wedge, and the subducting Nazca plate. The along-arc variations are significant in all these layers, which may result from differences in the age, dip angle, and fluid content of the subducting slab beneath the northern and southern segments.

In the Iquique segment (18°S–21°S), the subducting slab is older and therefore colder. The slab dip angle is ~25°. There is probably more fluid in the slab as a result of the Iquique ridge subduction. We revealed a pattern of radiating FVDs in the crust, likely reflecting the radiating horizontal extension directions in the crust, which may be caused by an isolated, highly locked asperity at the plate interface. The FVDs in the mantle wedge corner are trench parallel, which could reflect the mineral fabric under trench-normal compression or B-type olivine fabrics. The trench-normal FVDs dominant in the deeper mantle wedge were most likely caused by mantle wedge flow. Trench-normal FVDs are also notable in the subducting slab, which may reflect fossil anisotropy in the slab or alternatively result from trench-normal extension due to the slab bending in the upper part of the slab.

In the Tocopilla segment (21°S–23°S), the subducting slab is younger and its dip angle is low, only ~15°. The FVDs in the crust are mostly normal to the motion direction of the Nazca plate. The FVDs in the mantle wedge are trench normal, as expected from mantle wedge flow induced by slab drag. The FVDs in the subducting slab are trench parallel, different from the pattern in the Iquique segment. In other

subduction zones, trench parallel FVDs are often interpreted as evidence for the hydration (serpentinization) of the oceanic upper mantle along steeply dipping outer rise faults subparallel to the trench, leading to alternating subvertical layers of different velocities (e.g., Faccenda et al., 2008). This mechanism may explain the results in the Tocopilla segment, but in the Iquique segment the presence of the Iquique ridge complicates the formation of deeply penetrating outerrise faults with simple geometries. An alternative hypothesis is that the upper part of the subducting slab there has experienced subsequent unbending (even reverse bending) at depth after the slab bending near the trench. Thus, the trench-normal compression in the upper part of the slab induces the trench-parallel extension and mineral fabrics, which produces the trench-parallel anisotropy together with the aligned faults and cracks in the serpentinized slab.

Another important result is the FVD changes along the plate interface. The FVDs are trench parallel in the regions where the plate interface is highly or partly locked. The horizontal compression may dominate and produce the trench-parallel fabrics. In the deeper part without notable interplate locking, the active subduction induces continuous and stable shear deformation in the subduction thrust zone along the plate interface. The mineral fabrics in this case produce the trench-normal anisotropy there.

References

Allmendinger, R. W., & González, G. (2010). Neogene to Quaternary tectonics of the coastal Cordillera, northern Chile. *Tectonophysics*, *495*(1–2), 93–110. https://doi.org/10.1016/j.tecto.2009.04.019

Allmendinger, R. W., González, G., Yu, J., Hoke, G., & Isacks, B. (2005). Trench-parallel shortening in the Northern Chilean Forearc: Tectonic and climatic implications. *Bulletin of the Geological Society of America*, *117*(1), 89–104. https://doi.org/10.1130/B25505.1

Angermann, D., Klotz, J., & Reigber, C. (1999). Space-geodetic estimation of the Nazca-South America Euler vector. *Earth and Planetary Science Letters*, *171*(3), 329–334. https://doi.org/10.1016/S0012-821X(99)00173-9

Aron, F., Allmendinger, R. W., Cembrano, J., González, G., & Yáñez, G. (2013). Permanent fore-arc extension and seismic segmentation: Insights from the 2010 Maule earthquake, Chile. *Journal of Geophysical Research: Solid Earth*, *118*, 724–739. https://doi.org/10.1029/2012JB009339

Babuška, V., Plomerová, J., & Šílený, J. (1993). Models of seismic anisotropy in the deep continental lithosphere. *Physics of the Earth and Planetary Interiors*, *78*(3-4), 167–191. https://doi.org/10.1016/0031-9201(93)90154-2

Backus, G. E. (1965). Possible forms of seismic anisotropy of the uppermost mantle under oceans. *Journal of Geophysical Research*, *70*(14), 3429–3439. https://doi.org/10.1029/JZ070i014p03429

Becker, T. W., Chevrot, S., Schulte-Pelkum, V., & Blackman, D. K. (2006). Statistical properties of seismic anisotropy predicted by upper mantle geodynamic models. *Journal of Geophysical Research*, *111*, B08309. https://doi.org/10.1029/2005JB004095

Bedford, J., Moreno, M., Schurr, B., Bartsch, M., & Oncken, O. (2015). Investigating the final seismic swarm before the Iquique-Pisagua 2014 M-w 8.1 by comparison of continuous GPS and seismic foreshock data. *Geophysical Research Letters*, *42*, 3820–3828. https://doi.org/10.1002/2015GL063953

Bevis, M., Kendrick, E., Smalley, R., Brooks, B., Allmendinger, R., & Isacks, B. (2001). On the strength of interplate coupling and the rate of back arc convergence in the central Andes: An analysis of the interseismic velocity field. *Geochemistry, Geophysics, Geosystems*, *2*. https://doi.org/10.1029/2001GC000198

Bloch, W., Kummerow, J., Salazar, P., Wigger, P., & Shapiro, S. A. (2014). High-resolution image of the North Chilean subduction zone: Seismicity, reflectivity and fluids. *Geophysical Journal International*, *197*(3), 1744–1749. https://doi.org/10.1093/gji/ggu084

Bock, G., Kind, R., Rudloff, A., & Asch, G. (1998). Shear wave anisotropy in the upper mantle beneath the Nazca plate in northern Chile. *Journal of Geophysical Research*, *103*(B10), 24,333–24,345. https://doi.org/10.1029/98JB01465

Browaeys, J. T., & Chevrot, S. (2004). Decomposition of the elastic tensor and geophysical applications. *Geophysical Journal International*, *159*(2), 667–678. https://doi.org/10.1111/j.1365-246X.2004.02415.x

Chlieh, M., De Chabalier, J. B., Ruegg, J. C., Armijo, R., Dmowska, R., Campos, J., & Feigl, K. L. (2004). Crustal deformation and fault slip during the seismic cycle in the North Chile subduction zone, from GPS and InSAR observations. *Geophysical Journal International*, *158*(2), 695–711. https://doi.org/10.1111/j.1365-246X.2004.02326.x

Comte, D., Carrizo, D., Roecker, S., Ortega-Culaciati, F., & Peyrat, S. (2016). Three-dimensional elastic wave speeds in the northern Chile subduction zone: Variations in hydration in the supraslab mantle. *Geophysical Journal International*, *207*(2), 1080–1105. https://doi.org/10.1093/gji/ggw318

Comte, D., & Pardo, M. (1991). Reappraisal of great historical earthquakes in the northern Chile and southern Peru seismic gaps. *Natural Hazards*, *4*(1), 23–44. https://doi.org/10.1007/BF00126557

Cortés-Aranda, J., González, G., Rémy, D., & Martinod, J. (2015). Normal upper plate fault reactivation in northern Chile and the subduction earthquake cycle: From geological observations and static Coulomb Failure Stress (CFS) change. *Tectonophysics*, *639*, 118–131. https://doi.org/10.1016/j.tecto.2014.11.019

Crampin, S., & Peacock, S. (2005). A review of shear-wave splitting in the compliant crack-critical anisotropic Earth. *Wave Motion*, *41*(1), 59–77. https://doi.org/10.1016/j.wavemoti.2004.05.006

Dominguez, S., Lallemand, S., Malavieille, J., & von Huene, R. (1998). Upper plate deformation associated with seamount subduction. *Tectonophysics*, *293*(3–4), 207–224. https://doi.org/10.1016/S0040-1951(98)00086-9

Eakin, C. M., Long, M. D., Scire, A., Beck, S. L., Wagner, L. S., Zandt, G., & Tavera, H. (2015). Internal deformation of the subducted Nazca slab inferred from seismic anisotropy. *Nature Geoscience*, *9*(1), 56–59. https://doi.org/10.1038/ngeo2592

Eberhart-Phillips, D., & Henderson, C. M. (2004). Including anisotropy in 3-D velocity inversion and application to Marlborough, New Zealand. *Geophysical Journal International*, *156*(2), 237–254. https://doi.org/10.1111/j.1365-246X.2003.02044.x

Eberhart-Phillips, D., & Reyners, M. (2009). Three-dimensional distribution of seismic anisotropy in the Hikurangi subduction zone beneath the central North Island, New Zealand. *Journal of Geophysical Research*, *114*, B06301. https://doi.org/10.1029/2008JB005947

Engdahl, E. R., & Lee, W. H. K. (1976). Relocation of local earthquakes by seismic ray tracing. *Journal of Geophysical Research*, *81*(23), 4400–4406. https://doi.org/10.1029/JB081i023p04400

Faccenda, M., Burlini, L., Gerya, T. V., & Mainprice, D. (2008). Fault-induced seismic anisotropy by hydration in subducting oceanic plates. *Nature*, *455*(7216), 1097–1100. https://doi.org/10.1038/nature07376.

Gamage, S. S. N., Umino, N., Hasegawa, A., & Kirby, S. H. (2009). Offshore double-planed shallow seismic zone in the NE Japan forearc region revealed by sP depth phases recorded by regional networks. *Geophysical Journal International*, *178*(1), 195–214. https://doi.org/10.1111/j.1365-246X.2009.04048.x

Gephart, J. W. (1994). Topography and subduction geometry in the central Andes—Clues to the mechanics of a noncollisional orogen. *Journal of Geophysical Research*, *99*(B6), 12,279–12,288. https://doi.org/10.1029/94JB00129

GFZ German Research Centre for Geosciences; Institut des Sciences de l'Univers-Centre National de la Recherche CNRS-INSU (2006). IPOC seismic network. Integrated plate boundary observatory Chile—IPOC. Other/seismic network. doi:https://doi.org/10.14470/PK615318.

Graeber, F. M., & Asch, G. (1999). Three-dimensional models of P wave velocity and P-to-S velocity ratio in the southern central Andes by simultaneous inversion of local earthquake data. *Journal of Geophysical Research*, *104*(B9), 20,237–20,256. https://doi.org/10.1029/1999JB900037

Haberland, C., & Rietbrock, A. (2001). Attenuation tomography in the western central Andes: A detailed insight into the structure of a magmatic arc. *Journal of Geophysical Research*, *106*(B6), 11,151–11,167. https://doi.org/10.1029/2000JB900472

Hearn, T. M. (1996). Anisotropic Pn tomography in the western United States. *Journal of Geophysical Research*, *101*(B4), 8403–8414. https://doi.org/10.1029/96JB00114

Hicks, S. P., Nippress, S. E. J., & Rietbrock, A. (2012). Sub-slab mantle anisotropy beneath south-central Chile. *Earth and Planetary Science Letters*, *357-358*, 203–213. https://doi.org/10.1016/j.epsl.2012.09.017

Hu, J., Faccenda, M., & Liu, L. (2017). Subduction-controlled mantle flow and seismic anisotropy in South America. *Earth and Planetary Science Letters*, *470*, 13–24. https://doi.org/10.1016/j.epsl.2017.04.027

Huang, T. Y., Gung, Y., Kuo, B. Y., Chiao, L. Y., & Chen, Y. N. (2015). Layered deformation in the Taiwan orogen. *Science*, *349*(6249), 720–723. https://doi.org/10.1126/science.aab1879

Huang, Z., Zhao, D., & Liu, X. (2015). On the trade-off between seismic anisotropy and heterogeneity: Numerical simulations and application to Northeast Japan. *Journal of Geophysical Research: Solid Earth*, *120*, 3255–3277. https://doi.org/10.1002/2014JB011784

Huang, Z., Zhao, D., & Wang, L. (2011). Seismic heterogeneity and anisotropy of the Honshu arc from the Japan Trench to the Japan Sea. *Geophysical Journal International*, *184*(3), 1428–1444. https://doi.org/10.1111/j.1365-246X.2011.04934.x

Husen, S., Kissling, E., & Flueh, E. R. (2000). Local earthquake tomography of shallow subduction in north Chile: A combined onshore and offshore study. *Journal of Geophysical Research*, *105*(B12), 28,183–28,198. https://doi.org/10.1029/2000JB900229

Ishise, M., & Oda, H. (2005). Three-dimensional structure of P-wave anisotropy beneath the Tohoku district, northeast Japan. *Journal of Geophysical Research*, *110*, B07304. https://doi.org/10.1029/2004JB003599

Ji, S., Shao, T., Michibayashi, K., Oya, S., Satsukawa, T., Wang, Q., Zhao, W., et al. (2015). Magnitude and symmetry of seismic anisotropy in mica- and amphibole-bearing metamorphic rocks and implications for tectonic interpretation of seismic data from the southeast Tibetan Plateau. *Journal of Geophysical Research: Solid Earth*, *120*, 6404–6430. https://doi.org/10.1002/2015JB012209

Jung, H., & Karato, S.-I. (2001). Water-induced fabric transitions in olivine. *Science*, *293*(5534), 1460–1463. https://doi.org/10.1126/science.1062235.

Kaminski, É., & Ribe, N. M. (2002). Timescales for the evolution of seismic anisotropy in mantle flow. *Geochemistry, Geophysics, Geosystems*, *3*(8), 1. http://doi.org/10.1029/2001GC000222

Karato, S.-I., Jung, H., Katayama, I., & Skemer, P. (2008). Geodynamic significance of seismic anisotropy of the upper mantle: New insights from laboratory studies. *Annual Review of Earth and Planetary Sciences*, *36*(1), 59–95. https://doi.org/10.1146/annurev.earth.36.031207.124120

Kato, A., Fukuda, J., Kumazawa, T., & Nakagawa, S. (2016). Accelerated nucleation of the 2014 Iquique, Chile Mw 8.2 earthquake. *Scientific Reports*, *6*(1). https://doi.org/10.1038/srep24792

Kendrick, E., Bevis, M., Smalley, R. Jr., & Brooks, B. (2001). An integrated crustal velocity field for the central Andes. *Geochemistry, Geophysics, Geosystems*, *2*, 1066. https://doi.org/10.1029/2001GC000191

Kennett, B., Engdahl, E. R., & Buland, R. (1995). Constraints on seismic velocities in the Earth from travel-times. *Geophysical Journal International*, *122*(1), 108–124. https://doi.org/10.1111/j.1365-246X.1995.tb03540.x

Kneller, E. A., van Keken, P. E., Karato, S.-I., & Park, J. (2005). B-type olivine fabric in the mantle wedge: Insights from high-resolution non-Newtonian subduction zone models. *Earth and Planetary Science Letters*, *237*(3–4), 781–797. https://doi.org/10.1016/j.epsl.2005.06.049

Koulakov, I., Jakovlev, A., Wu, Y.-M., Dobretsov, N. L., El Khrepy, S., & Al-Arifi, N. (2015). Three-dimensional seismic anisotropy in the crust and uppermost mantle beneath the Taiwan area revealed by passive source tomography. *Journal of Geophysical Research: Solid Earth*, *120*, 7814–7829. https://doi.org/10.1002/2015JB012408

Kreemer, C., Blewitt, G., & Klein, E. C. (2014). A geodetic plate motion and Global Strain Rate Model. *Geochemistry, Geophysics, Geosystems*, *15*, 3849–3889. https://doi.org/10.1002/2014GC005407

Lees, J. M., & Crosson, R. S. (1989). Tomographic inversion for three-dimensional velocity structure at Mount St. Helens using earthquake data. *Journal of Geophysical Research*, *94*(B5), 5716–5728. https://doi.org/10.1029/JB094iB05p05716

Li, S., Moreno, M., Bedford, J., Rosenau, M., & Oncken, O. (2015). Revisiting viscoelastic effects on interseismic deformation and locking degree: A case study of the Peru-North Chile subduction zone. *Journal of Geophysical Research: Solid Earth*, *120*, 4522–4538. https://doi.org/10.1002/2015JB011903

Liu, X., & Zhao, D. (2016). Seismic velocity azimuthal anisotropy of the Japan subduction zone: Constraints from P and S wave travel times. *Journal of Geophysical Research: Solid Earth*, *121*, 5086–5115. https://doi.org/10.1002/2016JB013116

Liu, X., & Zhao, D. (2017). Depth-varying azimuthal anisotropy in the Tohoku subduction channel. *Earth and Planetary Science Letters*, *473*, 33–43. https://doi.org/10.1016/j.epsl.2017.05.034

Long, M. D., Biryol, C. B., Eakin, C. M., Beck, S. L., Wagner, L. S., Zandt, G., et al. (2016). Overriding plate, mantle wedge, slab, and subslab contributions to seismic anisotropy beneath the northern Central Andean Plateau. *Geochemistry, Geophysics, Geosystems*, *17*, 2556–2575. https://doi.org/10.1002/2016GC006316

Mainprice, D. (2007). Seismic anisotropy of the deep Earth from a mineral and rock physics perspective. In *Treatise on Geophysics* (Vol. 2, pp. 437–491). Amsterdam: Elsevier. https://doi.org/10.1016/B978-044452748-6/00045-6

Masson, F., & Delouis, B. (1997). Local earthquake tomography in northern Chile using finite-difference calculations of P-travel times. *Physics of the Earth and Planetary Interiors*, *104*(4), 295–305. https://doi.org/10.1016/S0031-9201(97)00067-8

Métois, M., Vigny, C., & Socquet, A. (2016). Interseismic coupling, megathrust earthquakes and seismic swarms along the Chilean sub-
duction zone (38°–18°S). *Pure and Applied Geophysics*, *173*(5), 1431–1449. https://doi.org/10.1007/s00024-016-1280-5

Mpodozis, C., Arriagada, C., Basso, M., Roperch, P., Cobbold, P., & Reich, M. (2005). Late Mesozoic to Paleogene stratigraphy of the Salar
de Atacama Basin, Antofagasta, northern Chile: Implications for the tectonic evolution of the Central Andes. *Tectonophysics*, *399*(1–4),
125–154. https://doi.org/10.1016/j.tecto.2004.12.019

Mueller, R. D., Sdrolias, M., Gaina, C., & Roest, W. R. (2008). Age, spreading rates, and spreading asymmetry of the world's ocean crust.
Geochemistry, Geophysics, Geosystems, *9*, Q04006. https://doi.org/10.1029/2007GC001743

Ortega-Culaciati, F., Becerra-Carreño, V. C., Socquet, A., Jara, J., Carrizo, D., Norabuena, E. O., et al. (2015). Imaging the seismic cycle in
the central Andean subduction zone from geodetic observations, *AGU Fall Meeting Abstracts*.

Paige, C. C., & Saunders, M. A. (1982). LSQR: An algorithm for sparse linear equations and sparse least squares. *ACM Transactions on
Mathematical Software (TOMS)*, *8*(1), 43–71. https://doi.org/10.1145/355984.355989

Pavlis, G. L., & Booker, J. R. (1980). The mixed discrete-continuous inverse problem: Application to the simultaneous determination of
earthquake hypocenters and velocity structure. *Journal of Geophysical Research*, *85*(B9), 4801–4810. https://doi.org/10.1029/
JB085iB09p04801

Plomerová, J., & Babuška, V. (2010). Long memory of mantle lithosphere fabric—European LAB constrained from seismic anisotropy.
Lithos, *120*(1-2), 131–143. https://doi.org/10.1016/j.lithos.2010.01.008

Polet, J., Silver, P. G., Beck, S., Wallace, T., Zandt, G., Ruppert, S., et al. (2000). Shear wave anisotropy beneath the Andes from the BANJO,
SEDA, and PISCO experiments. *Journal of Geophysical Research*, *105*(B3), 6287–6304. https://doi.org/10.1029/1999JB900326

Raitt, R. W., Shor, G. G., Francis, T. J. G., & Morris, G. B. (1969). Anisotropy of the Pacific upper mantle. *Journal of Geophysical Research*,
74(12), 3095–3109. https://doi.org/10.1029/JB074i012p03095

Reiss, M. C., Wölbern, I., & Rümpker, G. (2017). Complex seismic anisotropy beneath the IPOC stations of northern Chile, *EGU General
Assembly*.

Russo, R. M., & Silver, P. G. (1994). Trench-parallel flow beneath the Nazca plate from seismic anisotropy. *Science*, *263*(5150), 1105–1111.
https://doi.org/10.2307/2883416

Saillard, M., Audin, L., Rousset, B., Avouac, J. P., Chlieh, M., Hall, S. R., et al. (2017). From the seismic cycle to long-term deformation:
Linking seismic coupling and Quaternary coastal geomorphology along the Andean megathrust. *Tectonics*, *36*, 241–256. https://doi.org/
10.1002/2016TC004156

Savage, M. K. (1999). Seismic anisotropy and mantle deformation: What have we learned from shear wave splitting? *Reviews of Geophysics*,
37(1), 65–106. https://doi.org/10.1029/98RG02075

Schurr, B., Asch, G., Rietbrock, A., Trumbull, R., & Haberland, C. (2003). Complex patterns of fluid and melt transport in the central
Andean subduction zone revealed by attenuation tomography. *Earth and Planetary Science Letters*, *215*(1–2), 105–119. https://doi.org/
10.1016/S0012-821X(03)00441-2

Schurr, B., Asch, G., Rosenau, M., Wang, R., Oncken, O., Barrientos, S., et al. (2012). The 2007 M7.7 Tocopilla northern Chile earthquake
sequence: Implications for along-strike and downdip rupture segmentation and megathrust frictional behavior. *Journal of Geophysical
Research*, *117*, B05305. https://doi.org/10.1029/2011JB009030

Schurr, B., Rietbrock, A., Asch, G., Kind, R., & Oncken, O. (2006). Evidence for lithospheric detachment in the Central Andes from local
earthquake tomography. *Tectonophysics*, *415*(1–4), 203–223. https://doi.org/10.1016/j.tecto.2005.12.007

Sun, S. (2012). *Seismic velocities, anisotropy and elastic properties of crystalline rocks and implications for interpretation of seismic data*.
Montreal, Canada: Université de Montréal.

Sun, S., Ji, S., Wang, Q., Xu, Z., Salisbury, M., & Long, C. (2012). Seismic velocities and anisotropy of core samples from the Chinese
Continental Scientific Drilling borehole in the Sulu UHP terrane, eastern China. *Journal of Geophysical Research*, *117*, B01206. https://
doi.org/10.1029/2011JB008672

Tassara, A., & Echaurren, A. (2012). Anatomy of the Andean subduction zone: Three-dimensional density model upgraded and compared
against global-scale models. *Geophysical Journal International*, *189*(1), 161–168. https://doi.org/10.1111/j.1365-246X.2012.05397.x

Thurber, C. H. (1983). Earthquake locations and three-dimensional crustal structure in the Coyote Lake Area, central California. *Journal of
Geophysical Research*, *88*(B10), 8226–8236. https://doi.org/10.1029/JB088iB10p08226

Tommasi, A., Tikoff, B., & Vauchez, A. (1999). Upper mantle tectonics: Three-dimensional deformation, olivine crystallographic fabrics
and seismic properties. *Earth and Planetary Science Letters*, *168*(1–2), 173–186. https://doi.org/10.1016/S0012-821X(99)00046-1

Um, J., & Thurber, C. (1987). A fast algorithm for two-point seismic ray tracing. *Bulletin of the Seismological Society of America*, *77*(3),
972–986.

Wang, J., & Zhao, D. (2008). P-wave anisotropic tomography beneath Northeast Japan. *Physics of the Earth and Planetary Interiors*,
170(1–2), 115–133. https://doi.org/10.1016/j.pepi.2008.07.042

Wang, J., & Zhao, D. (2013). P-wave tomography for 3-D radial and azimuthal anisotropy of Tohoku and Kyushu subduction zones.
Geophysical Journal International, *193*(3), 1166–1181. https://doi.org/10.1093/gji/ggt086

Wei, W., Zhao, D., Xu, J., Wei, F., & Liu, G. (2015). P and S wave tomography and anisotropy in Northwest Pacific and East Asia:
Constraints on stagnant slab and intraplate volcanism. *Journal of Geophysical Research: Solid Earth*, *120*, 1642–1666. https://doi.org/
10.1002/2014JB011254

Wei, W., Zhao, D., Xu, J., Zhou, B., & Shi, Y. (2016). Depth variations of P-wave azimuthal anisotropy beneath Mainland China. *Scientific
Reports*, *6*(1). https://doi.org/10.1038/srep29614

Wessel, P., Smith, W. H. F., Scharroo, R., Luis, J., & Wobbe, F. (2013). Generic mapping tools: Improved version released. *Eos, Transactions
American Geophysical Union*, *94*(45), 409–410. https://doi.org/10.1002/2013EO450001

Wölbern, I., Löbl, U., & Rümpker, G. (2014). Crustal origin of trench-parallel shear-wave fast polarizations in the Central Andes. *Earth and
Planetary Science Letters*, *392*, 230–238. https://doi.org/10.1016/j.epsl.2014.02.032

Zhao, D., Hasegawa, A., & Horiuchi, S. (1992). Tomographic imaging of P and S wave velocity structure beneath northeastern Japan.
Journal of Geophysical Research, *97*(B13), 19,909–19,928. https://doi.org/10.1029/92JB00603

Zhao, D., Yu, S., & Liu, X. (2016). Seismic anisotropy tomography: New insight into subduction dynamics. *Gondwana Research*, *33*, 24–43.
https://doi.org/10.1016/j.gr.2015.05.008